

SDSS-IV MaNGA: global and local stellar population properties of elliptical galaxies

I. Lacerna^{1,2}, H. Ibarra-Medel³, V. Avila-Reese⁴, H. M. Hernández-Toledo⁴, J. A. Vázquez-Mata⁴, and S. F. Sánchez⁴

¹ Instituto de Astronomía y Ciencias Planetarias, Universidad de Atacama, Copayapu 485, Copiapó, Chile
e-mail: ivan.lacerna@uda.cl

² Instituto Milenio de Astrofísica, Av. Vicuña Mackenna 4860, Macul, Santiago, Chile

³ University of Illinois Urbana-Champaign, Department of Astronomy, 1002 W Green St, Urbana, Illinois, 61801, United States

⁴ Instituto de Astronomía, Universidad Nacional Autónoma de México, A.P. 70-264, 04510 México D. F., México

December 21, 2024

ABSTRACT

Context. We study the spatially resolved properties of 343 elliptical galaxies with the MaNGA/SDSS-IV survey.

Aims. Understanding the fundamental processes of formation and quenching of elliptical galaxies.

Methods. We used the DESI Legacy Imaging Surveys for accurate morphological classification. Based on integrated spectroscopic properties and colors, we classified seven classes of elliptical galaxies. We inferred the stellar age and metallicity gradients out to 1.5 effective radius (R_{eff}) of classical ‘red and dead’, recently quenched, and blue star-forming ellipticals (CLEs, RQEs, and BSFs corresponding to 73%, 10%, and 4% of the sample, respectively), and reconstructed their global and radial histories of star formation and mass growth.

Results. The mass- and luminosity-weighted age gradients of CLEs are nearly flat or mildly negative, with small differences between both ages. The respective metallicity gradients are negative ($\nabla \log[Z_{mu}] = -0.11^{+0.07}_{-0.08}$ dex/ R_{eff} and $\nabla \log[Z_{lw}] = -0.11^{+0.06}_{-0.07}$ dex/ R_{eff} , respectively), being flatter as less massive are the CLEs. The more massive CLEs formed stars earlier and quenched faster than the less massive ones. The CLEs show a weak inside-out growth and a clear inside-out quenching. They finished their quenching globally 3.8 ± 1.2 Gyr ago on average, with quenching time-scales of 3.4 ± 0.8 Gyr. At $M_{\star} < 10^{11} M_{\odot}$, the age and Z gradients of the RQEs and BSFs are flatter than those of the CLEs but with larger scatters. They show very weak inside-out growth and quenching, being the quenching slow and even not completed at $z \sim 0$ for the BSFs. Instead, the massive RQEs show an outside-in quenching and positive gradients in the luminosity-weighted age and stellar metallicities. The RQEs of all masses quenched 1.2 ± 0.9 Gyr ago on average.

Conclusions. Our results for the CLEs are consistent with a two-phase scenario where their inner parts formed by an early and coeval dissipative collapse with a consequent burst of star formation and further quenching, whereas the outer parts continued their assembly likely by dry mergers. We also discuss some evolutionary scenarios for the RQE and BSF galaxies that would agree with the generic results.

Key words. galaxies: elliptical and lenticular, cD - galaxies: formation - galaxies: evolution - galaxies: stellar content - galaxies: structure - galaxies: star formation

1. Introduction

Elliptical (E) galaxies are the earliest-type galaxies in the Hubble Tuning Fork diagram (Hubble 1936). For many decades they have been described as galaxies formed either in an intense early burst of star formation after a violent dissipative monolithic collapse (e.g., Larson 1974; Oemler 1974; White 1978) or assembled lately by dry mergers of fully formed galaxies (e.g., Toomre 1977; Dressler 1980; Hernquist 1993; Tutukov et al. 2007; Kormendy et al. 2009). In more recent years, these scenarios were modified in the light of the hierarchical clustering paradigm and the new observations. Es are proposed to form mainly in early collapsing high mass-density peaks, where the gaseous disks suffer wet mergers or strong gas feeding by cold streams and form stars intensively from the dissipated gas. After this violent process of star formation and gas consumption, feedback mechanisms and environmental conditions both avoid further gas accretion and quench star formation; a fraction of elliptical galaxies can continue significantly growing later by dry mergers (see for reviews, e.g., Mo et al. 2010; Kormendy 2016; and more references therein). This scenario motivated the concept of “red and

dead” galaxies to refer to Es (e.g., van Dokkum 2005; Bamford et al. 2009; Darg et al. 2010; Smith et al. 2010; Crossett et al. 2014; Davis & Bureau 2016; Boardman et al. 2017). The previous scenario offers a good representation for massive E galaxies. They dominate the morphological mix of galaxies for stellar masses higher than $\sim 10^{10.8} M_{\odot}$ (Gadotti 2009; Nair & Abraham 2010; Fisher & Drory 2011; Cibinel et al. 2013; Avila-Reese et al. 2014; Thanjavur et al. 2016).

With new instruments and more dedicated observations in this century, it has been possible to learn new details. In particular, the number of local early-type (i.e., E and lenticular) galaxies with integrated properties different to the classical “red and dead” massive ones increases as the stellar mass is smaller and the environment becomes less dense (e.g., Kuntschner et al. 2002; Bernardi et al. 2006; Lee et al. 2006; Schawinski et al. 2007; 2009; Kannappan et al. 2009; Suh et al. 2010; Thomas et al. 2010; McIntosh et al. 2014; Schawinski et al. 2014; George & Zingade 2015; Vulcani et al. 2015; Lacerna et al. 2016; Spector & Brosch 2017; Argudo-Fernández et al. 2018; Lacerna et al. 2018). Two examples of these early-type galaxies are the recently quenched ellipticals (RQEs) and the blue, star-forming

ellipticals (BSFs). [McIntosh et al. \(2014\)](#) defined the RQEs as mostly blue E galaxies at $z \leq 0.08$ with light-weighted stellar ages shorter than 3–4 Gyr and lack of detectable emission lines from star formation. They suggest them as candidates for ‘first-generation’ Es formed in a relatively recent spiral-spiral major merger. BSFs are blue galaxies with high star formation rates and light-weighted stellar ages lower than 1–2 Gyr, indicating recent processes of star formation in them ([Lacerna et al. 2016; 2018](#)).

Projects with Integral Field Spectroscopy (IFS; see for a recent review [Sánchez 2020](#)) based on Integral Field Units (IFUs) such as SAURON ([Bacon et al. 2001; de Zeeuw et al. 2002; Sarzi et al. 2006; Emsellem et al. 2007; Shapiro et al. 2010](#)), ATLAS^{3D} ([Cappellari et al. 2011a,b; Young et al. 2014](#)), CALIFA ([Sánchez et al. 2012; González Delgado et al. 2015; Aquino-Ortíz et al. 2018](#)), SAMI ([Croom et al. 2012; Bassett et al. 2017; Barone et al. 2018](#)), MASSIVE ([Ma et al. 2014; Veale et al. 2018](#)), and MaNGA ([Bundy et al. 2015; Blanton et al. 2017; Wake et al. 2017](#)) have revolutionized our understanding of early-type galaxies (E+S0) by resolving stellar populations and minimizing the effects of aperture size and slit losses. For example, [McDermid et al. \(2015\)](#) applied single stellar populations models and non-parametric star formation histories in early-type galaxies of ATLAS^{3D} and found that massive E+S0 galaxies formed 50% of their stars at $z \sim 3$. In contrast, low-mass E+S0 galaxies reach the same fraction of stars at $z \sim 0.6$. [Ibarra-Medel et al. \(2016\)](#) studied the stellar mass growth histories of galaxies in MaNGA and found that the inside-out formation mode is more pronounced, on average, in late-type galaxies than in early-type galaxies, independently of mass. [González Delgado et al. \(2017\)](#) (see also [García-Benito et al. 2017; López Fernández et al. 2018; Bitsakis et al. 2019](#)) studied the spatially resolved star formation histories (SFHs) in CALIFA and found that the star formation rate (SFR) in outer regions of E+S0 galaxies have undergone an extended phase of growth in mass between $z = 2$ and 0.4 (see also [Sánchez et al. 2019](#) for the SFHs of E+S0 galaxies in MaNGA). Besides, massive E galaxies show evidence of early and fast quenching of star formation, whereas less massive E galaxies show extended SFHs with slow quenching. The information provided by IFS has also been used to constrain the origin of the gas content and the assembly history of E+S0 galaxies in simulations ([Lagos et al. 2014; Naab et al. 2014](#); and references therein).

In this paper, we use data from MaNGA, so far, the largest IFS galaxy survey. Unlike other works on early-type galaxies in general, we will focus here on the spatially resolved properties of only E galaxies, i.e., not including evident S0 galaxies (see also [Domínguez Sánchez et al. 2019](#) and [Bernardi et al. 2019](#) with MaNGA), with a particular focus on classical (red and quenched) E galaxies, CLEs. The post-processing catalog from the DESI Legacy Imaging Surveys ([Dey et al. 2019](#)) allowed us to look for disk features and sharp edges in E galaxies, and then purify our sample to purely E galaxies as possible. On the other hand, given the spectral information provided by MaNGA, we can accurately select this kind of galaxies, excluding those with signatures of active star formation (SF) or active galactic nuclei (AGN), as well as those with blue colors. Here, we will use the spatially-resolved spectral analysis of the MaNGA CLEs to find constraints on the local and global SFH and stellar mass growth of these galaxies. In addition, we pay attention to other two particular, much less frequent E classes; the RQE and BSF galaxies. What mechanisms are behind the recent star formation quenching of RQEs? In the case of the BSFs, are they classic E galaxies

that were rejuvenated by recent cosmological gas accretion or wet minor mergers? Or are they post-starburst galaxies with recent morphological transformation?

We aim to carry out our explorations in terms of stellar mass and galaxy structural parameters. We study the profiles of specific SFR (sSFR), stellar ages, and stellar metallicities of classical E, RQE, and BSF galaxies, and reconstruct their cumulative temporal distributions of stellar mass and SF at two different radial regions using the IFUs of MaNGA. We present statistics and general results on the populations for the classical E, RQE, and BSF galaxies. In a companion paper, we will study the different properties presented here in terms of the environment and individual-based cases for the low-frequent populations of RQE and BSF galaxies.

The outline of the paper is as follows. Section 2 presents the description of MaNGA. This section also describes the visual morphological classification of E galaxies and their integrated and resolved physical properties used throughout the paper. In Sect. 3, we classify E galaxies based on integrated properties such as color, equivalent width of H α , light-weighted stellar age, emission lines of the BPT diagram, and total stellar mass. From this selection, we pay special attention to classical Es, RQEs, and BSFs and study their radial profiles and gradients in stellar age and metallicity in Sect. 4. We estimate their cumulative mass temporal distributions and SFHs, globally and radially, in Sect. 5, and determine the long-term quenching epoch and time-scale of the Es when it applies. The implications of our results are discussed in Sect. 6 and the conclusions are given in Sect. 7.

Throughout this paper the reduced Hubble constant, h , is defined as $H_0 = 71 \, h \, \text{km s}^{-1} \, \text{Mpc}^{-1}$, unless other value of h is specified, with the following dependencies: stellar mass in $h^{-2} \, \text{M}_\odot$, physical scale in $h^{-1} \, \text{Mpc}$, and age and look back time in $h^{-1} \, \text{yr}$. When a cosmological model should be assumed, we use a flat model with $\Omega_\Lambda = 0.73$; the age for this model is 13.67 Gyr.

2. Data

2.1. Sample

MaNGA (Mapping Nearby Galaxies at the Apache Point Observatory) is an IFS survey of galaxies in the redshift range $0.01 < z < 0.15$ on the SDSS 2.5 m telescope ([Gunn et al. 2006](#)). Each spectra has a wavelength coverage of 3600–10,300 Å, an instrumental resolution of $\sim 65 \, \text{km s}^{-1}$, and median spatial resolution of 2.54 arcsec FWHM (1.8 kpc at the median redshift of 0.037, [Drory et al. 2015; Law et al. 2015, 2016](#)). We use the MaNGA Product Launch-7 (MPL-7) from the Sloan Digital Sky Survey (SDSS) Data Release 15 ([Aguado et al. 2019](#)) that contains 4621 galaxies.

2.2. Stellar population analysis

We make use of the Pipe3D pipeline ([Sánchez et al. 2016a,b; 2018](#)) to perform the spatially resolved stellar population analysis of the data cubes. Pipe3D is based on the stellar population synthesis code FIT3D ([Sánchez et al. 2016a,b](#)) that uses the GRANADA and MILES simple stellar population (SSP) libraries in the current implementation to model and subtract the stellar spectrum and fit the emission lines. The GRANADA and MILES (gsd156) stellar library is a combination of the empirical stellar library of [Vazdekis et al. \(2010\)](#) and the theoretical stellar libraries of [González Delgado et al. \(2005\)](#) and [González Delgado & Cid Fernandes \(2010\)](#). The SSPs use a [Salpeter \(1955\)](#) initial mass function and cover 39 stellar ages (from 1 Myr to

14.1 Gyr¹) and 4 metallicities (Z=0.002, 0.008, 0.02, and 0.03). FIT3D performs the SSP fitting within the wavelength of 3500Å to 7000Å. In addition, FIT3D considers the effects on dust extinction during the stellar population synthesis using a Cardelli et al. (1989) extinction law. FIT3D provides the SSP decomposition of the modeled stellar spectra of each spatially resolved region of the galaxies. With this decomposition, we can estimate the respective SFHs and the Cumulative Mass Temporal Distributions (or mass growth histories; e.g., Ibarra-Medel et al. 2016; 2019; Sánchez et al. 2019). For estimating the contemporary (local and integrated) SFR values, we smooth the SFHs within a period of 30 Myr. These quantities are independent of SFR estimations that use the H α emission line flux. For star-forming galaxies, both estimates are very similar, showing that the SFR calculated in the last 30 Myr is related to massive young stars, contributing to the H α emission. For retired galaxies, the SFR calculated from the H α flux is likely overestimated because this flux is dominated by effects of post-AGB stars rather than of young stars (see, e.g., Bitsakis et al. 2019; Sánchez et al. 2019). However, in these galaxies, the SFR derived from the stellar population synthesis with Pipe3D should also be considered an upper limit. To fit the emission lines, Pipe3D subtracts the modeled stellar spectra and fits a series of Gaussian profiles for each line (Sánchez et al. 2016b). With those fits, Pipe3D provides the total flux, dispersion, and the kinematics of each emission line. The quality of the emission line fits of Pipe3D (and other codes) was tested using MUSE data (Sánchez-Menguiano et al. 2018; Belllocchi et al. 2019; López-Cobá et al. 2020). By the use of the adjacent continuum windows (from the modeled stellar spectra) for each emission line, Pipe3D estimates the stellar continuum flux and provides the equivalent width of each emission line.

We estimate the integrated (within 1.5 effective radius, R_{eff}) and radially resolved (within a given radial region) luminosity- and mass-weighted stellar ages, age_{lw} and age_{mw} , respectively, using the following definitions:

$$\log(age_{mw}) = \sum_j^{n_{ssp}} \log(age_{ssp,j}) m_{ssp,j} / \sum_j^{n_{ssp}} m_{ssp,j}, \quad (1)$$

$$\log(age_{lw}) = \sum_j^{n_{ssp}} \log(age_{ssp,j}) L_{ssp,j} / \sum_j^{n_{ssp}} L_{ssp,j}, \quad (2)$$

where $age_{ssp,j}$ is the single stellar population age with index j , luminosity $L_{ssp,j}$, and mass $m_{ssp,j}$; n_{ssp} is the total number of SSPs within 1.5 R_{eff} or the given radial region. We calculate in the same way the respective mass- and luminosity-weighted stellar metallicities, Z_{mw} and Z_{lw} . We also calculate the integrated and azimuthally-averaged radial surface-density values of the sSFR based on the stellar population synthesis method. We also calculate the following integrated quantities within 1.5 R_{eff} : H α equivalent width, and the emission line fluxes of H α , H β , [OIII] $\lambda 5007$, and [NII] $\lambda 6584$. The latter quantities are used to study the BPT diagram (Baldwin et al. 1981; Veilleux & Osterbrock 1987; Kewley et al. 2001).

2.3. Morphology

A detailed description of the procedures in our visual classification of MPL-7 galaxies can be found in Vázquez-Mata et al. (in prep. See also Hernández-Toledo et al. 2008; 2010). Briefly, the

classification of each MaNGA galaxy was carried out by visually inspecting post-processed images from the SDSS and the DESI Legacy Imaging Surveys (Dey et al. 2019) in various stages.

A first input morphological evaluation was achieved by visually inspecting all the *gri* color images available in the SDSS image server. In a second stage, we used the Montage software packages from NASA/IPAC (Infrared Processing and Analysis Center) to re-assemble the *r*-band SDSS images corresponding to each MaNGA galaxy. These new background-subtracted and gradient-removed images were used to generate mosaics containing gray logarithmic-scaled *r*-band images and filter-enhanced *r*-band images (after applying Gaussian filters of various sizes that later were subtracted to the original images).

The DESI Legacy Imaging Surveys² have delivered optical images for an important fraction of the extragalactic sky visible from the northern hemisphere in three optical bands (*g*, *r*, and *z*), providing a survey of nearly uniform depth (5 σ depths of $g = 24.0$, $r = 23.4$, and $z = 22.5$ AB mag for a fiducial DESI point source). The DESI collaboration generated a post-processing catalog for the Legacy Surveys using an approach to estimate the light distribution, namely, source shapes and brightness properties. Each source was modeled using The Tractor package (see for more details Dey et al. 2019) using parametric light profiles, including, delta functions (for point sources); de Vaucouleurs (R/R_{eff})^{1/4} law; exponential disk; or composite de Vaucouleurs plus exponential. The best fit model was determined by convolving each model with the specific point spread function (PSF) for each exposure, fitting each image, and minimizing the residuals for all images. Similar to the SDSS images, the DESI legacy images for all MaNGA galaxies in the *r*-band were retrieved and digitally-processed to generate new mosaics containing filter-enhanced images, the *grz* color images and the corresponding residual images.

Early-type galaxies were classified according to their bulge dominance. Bulge-dominated galaxies have bright centers with a gradual fall-off in brightness at all radii, with the outer regions having an extended envelope without any sharp edges. On the other hand, disk-dominated galaxies have a sharp outer edge where the light drops off drastically, showing a flatter profile at intermediate radii. The disk can be either featureless or weakly featured (smooth disks) or with more defined or strong features (non-smooth disks).

Since a relevant goal for the present work is to isolate as much as possible between early-type E and S0 candidates, we did this separation by combining our previous experience (Hernández-Toledo et al. 2008; 2010) with a well-defined purely light-based approach by Cheng et al. (2011), in which red sequence galaxies are accommodated according to their light smoothness distribution into bulges, smooth disks, and non-smooth disks. Then, we assigned these groups to the Hubble types E, S0, and S0a, respectively. We explicitly notice that our bulge-dominated category is not composed of pure bulges. In our experience with the mosaic images, many apparent bulge-dominated galaxies have characteristics indicating the presence of both bulge and disk-like components like in galaxies showing a disk embedded within a more extended classical bulge (c.f., Cappellari et al. 2011b). In our classification, bulges with centrally concentrated disks or inner disks were classified as Es. On the other hand, galaxies, where the apparent disk (either face-on or edge-on) is occupying a significant (or dominant) fraction of the extended bulge, were classified as lenticulars, resembling the classification grid by Graham (2019) for early-type galaxies,

¹ In practice, we use results until 13 Gyr.

² <http://legacysurvey.org/>

and others including edge-on S0 galaxies. At present, only the most evident S0 cases were eliminated from our sample. In this way, we identify 539 E galaxies, which is $\approx 12\%$ of the MaNGA MPL-7 sample.

We emphasize that both our filter-enhanced and the PSF-convolved residual images from the DESI post-processing catalog were helpful to visually identify disk-like features and sharp edges in E galaxy candidates, and look for disk-features (broad/tight arm-like features) in S0 candidates including flattened edge-on disks. The depth of the DESI r -band images translates into a median surface brightness limit of ~ 27.5 mag arcsec $^{-2}$ for a 3σ detection of a 100 arcsec $^{-2}$ low surface brightness feature (Hood et al. 2018). In spite of the higher depth of the DESI images, a major limitation in our visual classification is the difficulty of classifying small or compact galaxies that show no visible structure or that cannot be resolved. Furthermore, the visual nature still allows for possible contamination of the E sample by face-on S0s. Domínguez Sánchez et al. (2020) recently found evidence that (fast-rotating) E galaxies are not simply S0 galaxies viewed face-on. In our experience, a more quantitative approach from an isophotal analysis as shown in Hernández-Toledo et al. (2008; 2010) in combination with a detailed 2D parametric decomposition of the DESI images are useful to identify possible face-on S0 galaxies.

2.4. Color, stellar mass, redshift, structural and kinematic properties

Color measurements were taken from the SDSS database with extinction corrected *modelMag* magnitudes (dered parameter in SkyServer³). This magnitude is defined as the better of two magnitude fits: a pure de Vaucouleurs profile and a pure exponential profile.

The stellar mass and redshift are obtained from the MaNGA Data Reduction Pipeline (DRP; Law et al. 2016). DRP includes galaxy properties from the NASA-Sloan Atlas (NSA⁴). For the stellar mass, we use *NSA_Sersic_MASS* that is calculated from a K-correction fit for Sérsic fluxes (two-dimensional Sérsic fit flux using r -band structural parameters). We find a good agreement between this definition of stellar mass and the stellar mass estimated with the stellar mass-to-light ratio of Bell et al. (2003), considering a Kroupa (2001) initial mass function (IMF), and including an extra correction to the Petrosian magnitudes of -0.1 mag since these magnitudes underestimate the total flux for E galaxies (Bell et al. 2003; McIntosh et al. 2014).

We use the Sérsic index and the concentration as two structural properties of E galaxies. The Sérsic index (n) is a two-dimensional, single-component Sérsic fit in the r -band and obtained from the NSA catalog (v1_0_1). The concentration is defined as R_{90}/R_{50} , where R_{90} and R_{50} are the azimuthally-averaged 90% and 50% light radius in Petrosian magnitudes, respectively, in the r -band. They are also obtained from the NSA catalog. We also calculate the ellipticity as $\epsilon = 1 - b/a$, in which the axis ratio b/a is a two-dimensional, single-component Sérsic fit in r -band from the NSA catalog.

For the kinematics, we calculate λ_{R_e} , the specific angular momentum for the stellar populations within $1 R_{eff}$, using the Pipe3D pipeline.

We establish an upper limit of $z = 0.08$ in our sample as a compromise to have a considerable number of galaxies with reliable visual morphological classifications of E galaxies, avoid

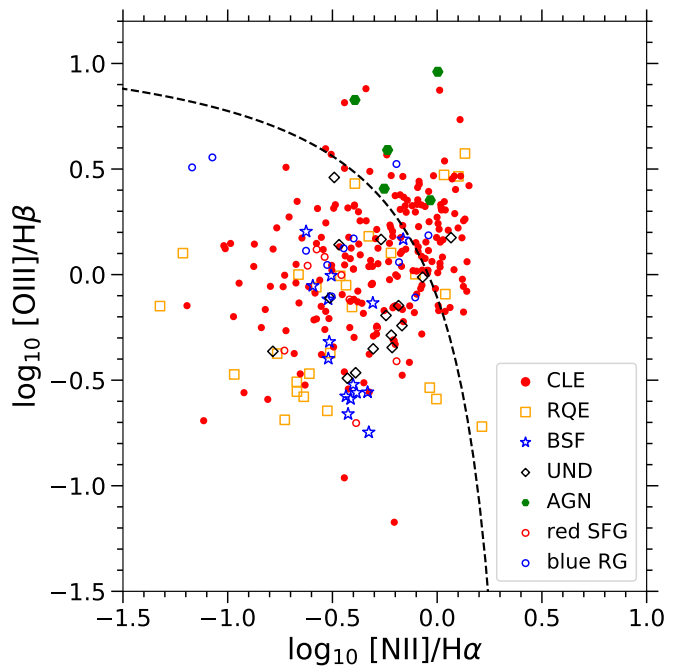


Fig. 1. BPT diagram of elliptical galaxies from MaNGA. The dashed line is given by Kewley et al. (2001). The symbols correspond to classical elliptical (CLE) galaxies in red filled circles, recently quenched elliptical (RQE) galaxies in orange open squares, blue and star-forming (BSF) elliptical galaxies in blue open stars, undetermined (UND) elliptical galaxies in black open diamonds, AGN elliptical galaxies in green filled hexagons, red star-forming ellipticals in red open circles, and blue retired galaxies (RG) in blue open circles. See the details of their classification in Sect. 3.

an excess of very red, massive galaxies that increase significantly in number at larger redshifts in MaNGA, and obtain a reasonable normalization of the cumulative mass temporal distributions at look back time ~ 1 Gyr (e.g., Bamford et al. 2009; Hernández-Toledo et al. 2010; Lacerna et al. 2014; Ibarra-Medel et al. 2016; Sánchez et al. 2017). We obtain 345 E galaxies out to $z = 0.08$. Finally, we adopt a lower limit in the stellar mass of $10^9 M_\odot$ to have a reliable sample. There are 343 E galaxies that satisfy this condition, with a median z of 0.044. This is our final sample of E galaxies.

3. Classification of elliptical galaxies based on their integrated properties

Following Sánchez et al. (2014) and Cano-Díaz et al. (2016); Cano-Díaz et al. (2019; and more references therein), we define the retired galaxies (RGs) as those galaxies with equivalent width (EW) of $H\alpha < 3$ Å. There are 299 RGs in our sample of E galaxies. The RQE galaxies are defined here as galaxies with $age_{lw} \leq 4$ Gyr and either RGs or with $3 \leq EW(H\alpha)/\text{Å} < 6$ lying above the relation of Kewley et al. (2001) in the BPT diagram (Fig. 1). We identify 35 RQEs, which are shown as orange open squares in Figs. 1–5. The RQEs are all RGs with young stellar populations. The other galaxies with $3 \leq EW(H\alpha) < 6$ Å and that are not classified as RQEs because lie below the Kewley et al. (2001) line, are nominally defined as undetermined (UND) E galaxies. There are 15 UND galaxies. Following Cano-Díaz et al. (2019), we define as star-forming galaxies (SFGs) and galaxies with active galactic nuclei (AGN) those systems that fall below

³ See <https://skyserver.sdss.org/dr15/>

⁴ See <http://nsatlas.org/>

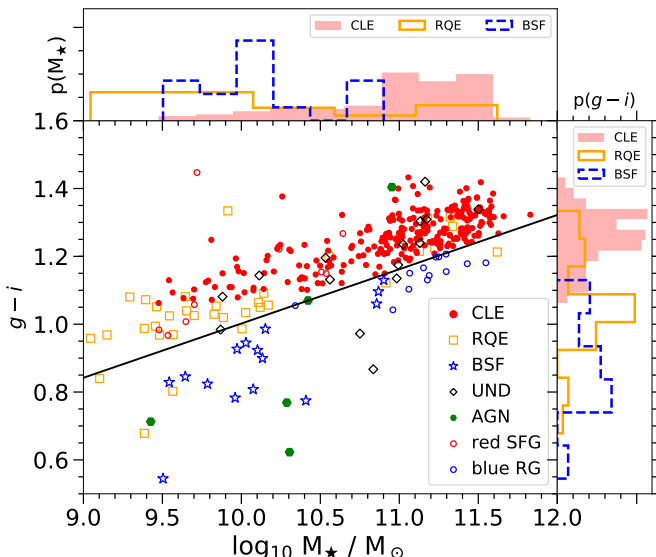


Fig. 2. As a function of stellar mass, $g - i$ color for E galaxies from MaNGA. The black solid line separates red and blue galaxies. The symbols for the galaxies are the same as Fig. 1. Top and right panels: normalized density distributions of stellar mass and $g - i$ color, respectively, for CLE galaxies (red solid histogram), RQE galaxies (orange open histogram), and BSF galaxies (blue dashed histogram). The integral of each histogram sums to unity.

and above the relation of Kewley et al. (2001; dashed line), respectively, and whose $\text{EW}(\text{H}\alpha) \geq 6 \text{ \AA}$. There are 24 SFGs and 5 AGNs.

Fig. 2 shows the $g - i$ color as a function of stellar mass. We use the relation found by Lacerna et al. (2014) to separate between red and blue galaxies (black solid line in the figure). The color is a representation of the aging of galaxies. RQEs are typically in the transition between red and blue galaxies. Therefore, our RQEs are a reliable sample of galaxies that stopped the star formation activity recently.

We find 251 RGs with red colors and not classified as RQEs (i.e., with $\text{age}_{lw} > 4 \text{ Gyr}$). We will refer to this population as classical elliptical (CLE) galaxies (red filled circles in Figs. 1–5). There are other 13 RG with blue colors and $\text{age}_{lw} > 4 \text{ Gyr}$. From the sample of SFGs, we identify 15 blue galaxies that we will refer to them as blue and SF (BSF) galaxies (blue open stars in Figs. 1–5). There are other 9 SFGs with red colors. The numbers and classification criteria of the E galaxies are summarized in Table 1.

The stellar mass (M_\star) distributions of BSFs and RQEs are different compared with the distribution of CLEs, as shown in the top panel of Fig. 2. CLEs are typically more massive with a median M_\star of $10^{11.1} M_\odot$, whereas the median M_\star is $10^{10.1} M_\odot$ for BSFs and $10^{9.9} M_\odot$ for RQEs. The latter presents a nearly flat mass distribution below $10^{10} M_\odot$. As mentioned above, the percentage of E galaxies with different properties than CLEs increases for lower masses (see also Lacerna et al. 2016). The CLEs correspond to 86% of the galaxies with $M_\star \geq 10^{11} M_\odot$, whereas RQEs are only ~4%, and none BSF is in this massive bin. For the range $10^{10.4} \leq M_\star < 10^{11} M_\odot$, CLEs are 78%, RQEs are ~4% and BSFs are ~5%. The change in the fractions is more important for lower masses, $M_\star < 10^{10.4} M_\odot$, where the CLEs are only 44%, RQEs are 29%, and BSFs are 12%. At $M_\star \leq 10^{9.4} M_\odot$ there are only RQE galaxies. The overall fractions reported in Table 1 should be taken with caution, given that our MaNGA

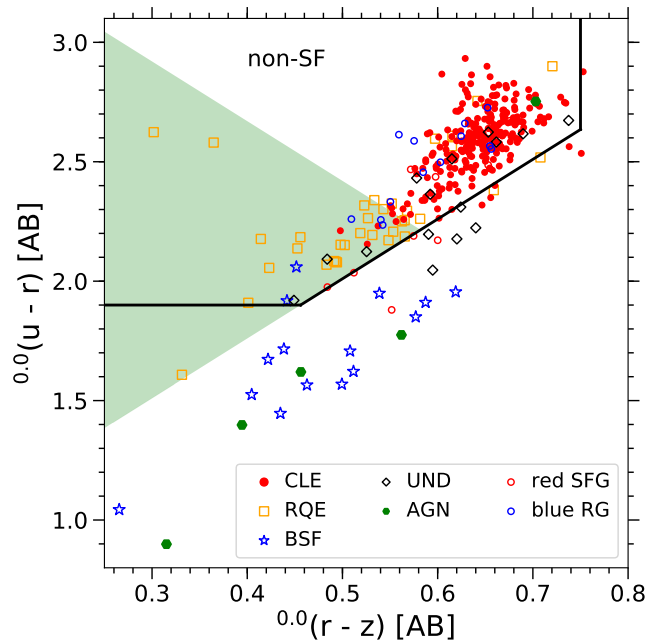


Fig. 3. Color–color diagram. The colors are in AB magnitudes and K -corrected at $z = 0$. The symbols for the galaxies are the same as Fig. 1. The thick black lines enclose the non-star-forming region of McIntosh et al. (2014) based on Holden et al. (2012). The green shaded region corresponds to an empirical relation to select RQE galaxies defined by McIntosh et al. (2014).

sample of Es is not from a complete volume survey. The fractions reported for each stellar mass bin are less affected by the volume incompleteness.

The $g - i$ color is also different between CLEs and BSFs by definition. The median $g - i$ color is 1.26 for the former and 0.90 for the latter. The RQEs are in the middle (median $g - i$ color of 1.05), with an overlap of the BSF and CLE color distributions. The definition of McIntosh et al. (2014) strongly motivates our classification of RQE galaxies. Following, we mention some differences. First, they use light-weighted median stellar ages $\leq 3 \text{ Gyr}$ derived by Gallazzi et al. (2005), whereas this upper limit is slightly relaxed to 4 Gyr in our case using integrated values of age_{lw} within $1.5 R_{eff}$ as described in Sect. 2.2. Second, they follow the method of Peek & Graves (2010) to define spectroscopically quiescent galaxies within an ellipse of $\text{EW}(\text{H}\alpha)$ and $\text{EW}(\text{OII})$ using fluxes from the Max Plank Institute for Astrophysics and Johns Hopkins University (MPA-JHU, Kauffmann et al. 2003; Brinchmann et al. 2004; Tremonti et al. 2004; Salim et al. 2007) catalog. Additionally, they consider quiescent galaxies those with $\text{S/N} < 3$ in $\text{H}\alpha$ flux or with $\text{EW}(\text{H}\alpha) \leq 2 \text{ \AA}$. In our case, we use the definition of RGs, i.e., $\text{EW}(\text{H}\alpha) < 3 \text{ \AA}$ integrated within $1.5 R_{eff}$, as the criterion for quiescent galaxies. Finally, RQE candidates are inside the non-star-forming region of the urz diagram according to McIntosh et al. (2014). We do not use this condition because we consider that our condition for RGs is good enough to select non-star-forming galaxies. Fig. 3 shows the urz diagram for our sample of E galaxies. Nearly all the RQEs using our selection criteria are located inside the modified non-star-forming region of McIntosh et al. (2014). We also include the empirical selection of RQE galaxies proposed by them using only the urz diagram, which is shown as a green shaded region. We find 25 (71%) of the RQEs using our selection criteria are located within this region. This fraction is smaller

Table 1. Classification of E galaxies.

type	N (%)	criteria
CLE	251 (73.2%)	$\text{age}_{lw} > 4 \text{ Gyr}$, $\text{EW}(\text{H}\alpha) < 3 \text{ \AA}$ and red
RQE	35 (10.2%)	$\text{age}_{lw} \leq 4 \text{ Gyr}$ and $\text{EW}(\text{H}\alpha) < 3 \text{ \AA}$
BSF	15 (4.4%)	$\text{EW}(\text{H}\alpha) \geq 6 \text{ \AA}$, below Kewley et al. (2001) line and blue
AGN	5 (1.4%)	$\text{EW}(\text{H}\alpha) \geq 6 \text{ \AA}$ and above Kewley et al. (2001) line
UND	15 (4.4%)	$3 < \text{EW}(\text{H}\alpha) \leq 6 \text{ \AA}$
blue RG	13 (3.8%)	$\text{age}_{lw} > 4 \text{ Gyr}$, $\text{EW}(\text{H}\alpha) < 3 \text{ \AA}$ and blue
red SFG	9 (2.6%)	$\text{EW}(\text{H}\alpha) \geq 6 \text{ \AA}$, below Kewley et al. (2001) line and red

Notes. Columns are the type of E galaxy, the number and percentage of each type and the criteria to classify them.

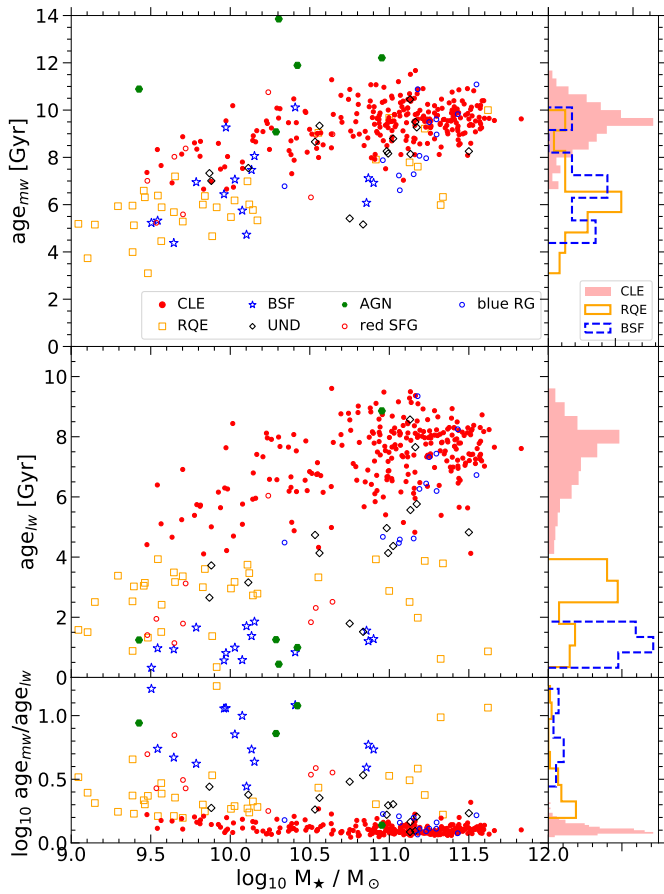


Fig. 4. Global mass-weighted stellar ages (top-left panel) and global luminosity-weighted stellar ages (middle-left panel) as functions of the stellar mass of E galaxies. The symbols for the galaxies are the same as Fig. 1. The relative difference between both ages is shown in the bottom-left panel. Top-right, middle-right, and bottom-right panels: normalized density distributions of mass-weighted ages, luminosity-weighted ages, and the relative difference between both ages, respectively, for CLE galaxies (red solid histogram), RQE galaxies (orange open histogram), and BSF galaxies (blue dashed histogram). The integral of each histogram sums to unity.

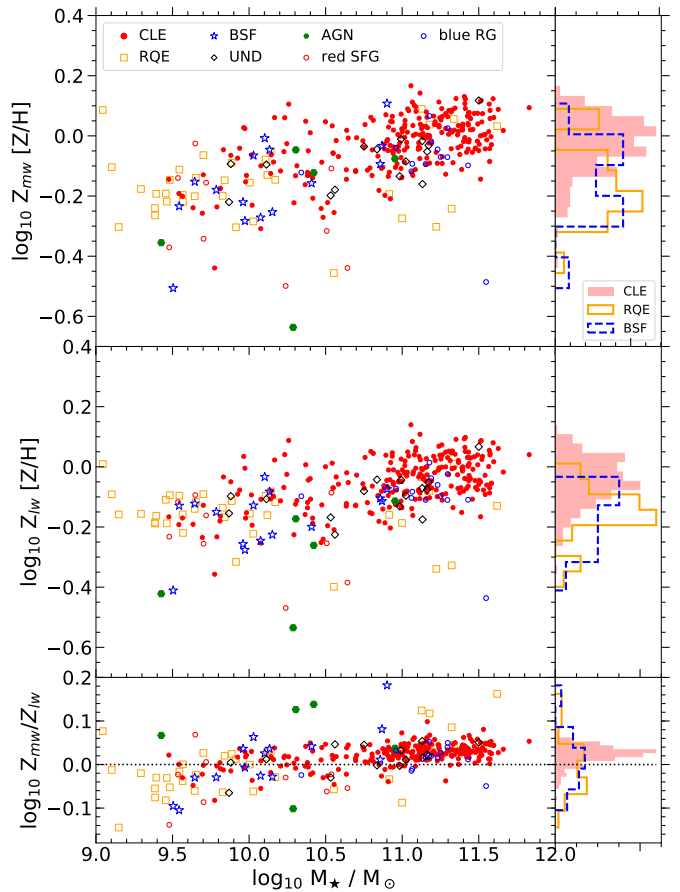


Fig. 5. Global mass-weighted stellar metallicities (top-left panel) and global luminosity-weighted stellar metallicities (middle-left panel) as functions of the stellar mass of E galaxies. The symbols for the galaxies are the same as Fig. 1. The relative difference between both metallicities (in dex units) is shown in the bottom-left panel. Top-right, middle-right, and bottom-right panels: normalized density distributions of mass-weighted Z, luminosity-weighted Z, and the relative difference between both Z, respectively, for CLE galaxies (red solid histogram), RQE galaxies (orange open histogram), and BSF galaxies (blue dashed histogram). The integral of each histogram sums to unity. The dotted line in the bottom panels is the difference in Z equals 0.

than the 82% of RQEs identified by [McIntosh et al. \(2014\)](#) with their empirical method, but it is expected given the different criteria mentioned above. We also find inside this empirical region 6 (2%) CLEs, 2 (13%) BSFs, 3 (20%) UNDs, 3 (23%) blue RGs, 1 (11%) red SFG, and none AGN. In summary, the [McIntosh et al. \(2014\)](#) empirical selection can identify a high fraction of

RQEs and includes mild pollution of other Es, especially from blue RGs and UNDs.

One of our aims is to explore whether the RQE galaxies, as defined here, are a distinct class of Es with respect to the CLEs, or they are just the expected tails in the color or age distribution

of the CLE galaxies. Based on our results, we will discuss it in Sect. 6.3.1.

Figure 4 shows the integrated (within $1.5 R_{\text{eff}}$) mass- and light-weighted stellar ages. The mass-weighted ages of CLEs are old, with a median of 9.5 Gyr, and a narrow distribution; CLEs less massive than $\sim 3 \times 10^{10} M_{\odot}$ are younger as less massive they are. The mass-weighted ages of the RQEs and BSFs are significantly younger and present much broader distributions than the CLEs, with medians of 6.0 and 6.9 Gyr, respectively, and not a clear trend with M_{\star} . Regarding the luminosity-weighted ages, the CLEs have a median age_{lw} of 7.5 Gyr. The RQEs are younger than 4 Gyr by definition, with a median age_{lw} of 3.0 Gyr. The BSFs present the youngest ages, with a median age_{lw} of 1.0 Gyr, which suggests recent episodes of star formation. Note that the luminosity-weighted age is more sensitive to small fractions of recent generations of stars (which contribute significantly in luminosity but little in mass), while the mass-weighted age represents better the average epoch when the bulk of the stars formed. Therefore, the (age_{mw}–age_{lw}) difference measures how coeval or dispersed in time was the SFH of a galaxy, and has been proposed as an estimator of the star formation timescale (Plauchu-Frayn et al. 2012). If the difference is big, it is because either the SFH is very extended or at least two different populations compose the current stellar populations, one dominant in mass formed early and the other formed much later. According to the bottom panels of Fig. 4, most of the CLEs have small (age_{mw}–age_{lw}) differences (around 2 Gyr on average and ~ 2.5 Gyr for the less massive galaxies) with median relative differences of 0.1 dex, suggesting that the star formation in CLEs was early and nearly coeval. This is not the case for the RQE and BSF galaxies. For RQEs, the differences are typically larger than 2 Gyr (median relative differences of 0.3 dex for RQE galaxies more massive than $10^{9.4} M_{\odot}$) and with a large scatter, especially for the more massive galaxies. The BSFs show the largest differences in (age_{mw}–age_{lw}), from ~ 3 Gyr to 9 Gyr with median relative differences of 0.7 dex, a clear signal of very recent episodes of star formation. Due to the uncertainties in the method explained in Sect. 6.1, the differences between both ages are lower limits.

Figure 5 shows the integrated (within $1.5 R_{\text{eff}}$) mass- and luminosity-weighted stellar metallicities. The CLEs are the most metal-rich E galaxies on average, and they present a trend of lower metallicities as smaller is M_{\star} . The relative ($Z_{\text{mw}}/Z_{\text{lw}}$) differences are small in these galaxies (around 0.025 dex on average for $M_{\star} \gtrsim 10^{10.4} M_{\odot}$, and around 0 dex for the less massive galaxies), showing that their stellar populations are rather homogeneous not only in age but also in metallicity. The trend with mass could be because younger populations in more massive galaxies came from late minor mergers with slightly younger, less metallic galaxies. This effect with the mass seems to have been more pronounced for the most massive RQEs, which show the largest ($Z_{\text{mw}}/Z_{\text{lw}}$) positive differences. Interestingly enough, for most of the less massive RQEs, Z_{lw} is slightly higher than Z_{mw} , suggesting that the young stellar populations formed from slightly more enriched gas. This ($Z_{\text{mw}}/Z_{\text{lw}}$) difference is also present for the less massive BSFs. Due to the uncertainties in the method explained in Sect. 6.1, the differences between both metallicities are lower limits.

3.1. Global structural and kinematic properties

We show two structural properties of the E galaxies in Fig. 6: the Sérsic index (n) in the two left panels and the i -band concentration (R_{90}/R_{50}) in the two right panels. The CLEs have a

strong peak at the largest value of $n = 6$. The RQE galaxies have a wider distribution of the Sérsic index. Their median values of n increases with stellar mass and correspond to bulge-dominated systems ($n > 2.5$). The BSFs also show a wide distribution of the Sérsic index, but the median values of n decrease with stellar mass. They also exhibit values of bulge-dominated systems. On the other hand, the median concentration is roughly independent of stellar mass up to $10^{10.5} M_{\odot}$ for the three subsamples of Es and tends to increase for larger masses for the CLEs. They are typically more concentrated than BSFs and RQEs with an overall median R_{90}/R_{50} of 3.3 compared with medians of 3.0 and 2.9 for BSFs and RQEs, respectively, except the most massive RQE with $R_{90}/R_{50} = 3.8$. The median values at all the masses are larger than 2.6, which is a usual limit to define early-type morphologies in the literature (e.g., see Strateva et al. 2001; McIntosh et al. 2014).

Figure 7 shows the $\lambda_{R_e} - \epsilon$ diagram (Emsellem et al. 2007; 2011), for the kinematic classification of our samples of morphological E galaxies. See, e.g., Graham et al. (2018), Smethurst et al. (2018), Tabor et al. (2019) and Bernardi et al. (2019) about this kinematic classification for MaNGA galaxies. The galaxies enclosed by the black lines correspond to non-regular rotators (i.e., slow rotators) according to Cappellari (2016). We find that nearly all the Es have low values of ϵ with a median value of 0.14. There is a wide distribution of λ_{R_e} . The peak is lower than $\lambda_{R_e} = 0.2$ for the CLEs, with a median of 0.17. The RQEs are the subsample of Es that show the highest values, i.e., more extended tails, of both ϵ and λ_{R_e} , with median values of $(\epsilon, \lambda_{R_e}) = (0.14, 0.34)$. Some signatures of a late morphological transformation may still be present in their kinematics. In the case of the BSFs, they have median values of $(\epsilon, \lambda_{R_e}) = (0.08, 0.25)$. Almost all the BSFs present a disk-like central structure (see Appendix C), which may explain the relatively high values of λ_{R_e} .

4. Radial profiles

This section presents information related to radial trends of the age, stellar metallicity, and sSFR obtained from the IFU spatially-resolved observations of the E galaxies defined as CLEs, RQEs, and BSFs. We first present the “stacked” radial profiles in three mass bins (Sect. 4.1). In Sect. 4.2 we present the scatter plots of the individual age and metallicity gradients for each galaxy as functions of the stellar mass. In these plots, rather than average radial trends of the population, we see the gradient that each galaxy has, and can evaluate then the fraction of galaxies that follow or not follow the average (stacked) trends.

4.1. The stacked radial profiles

To generate the “stacked” radial profiles, we first calculate the individual radial profiles for the given quantity in the same way described in Ibarra-Medel et al. (2019). We azimuthally average the 2D maps of each galaxy at five radial bins in terms of R_{eff} ⁵. We estimate the best linear fit of the stacked profiles by randomly resampling one thousand times each. The distribution of the resampling profiles follows the standard deviation and mean

⁵ For calculating the azimuthally-averaged radial profiles, we use only five radial bins in units of R_{eff} of the given galaxy because the typical PSF size of MaNGA observations does not allow for better resolving galaxies (see the horizontal error bars in panels of Figs. 8–10). In any case, we have also calculated the radial profiles using twelve radial bins, and find both the individual and “stacked” profiles are in most of the cases very similar to those using five radial bins (see Appendix B).

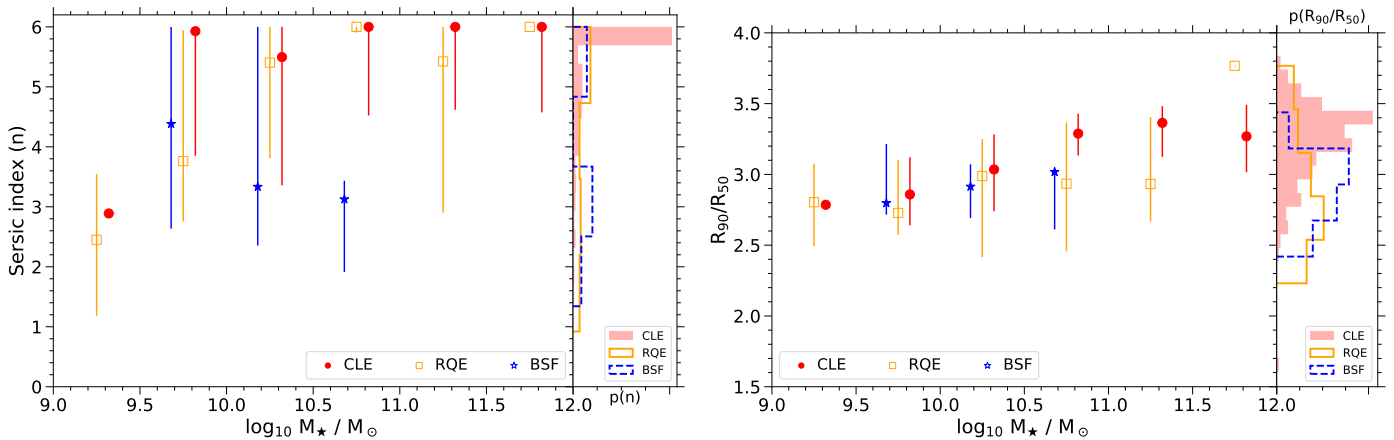


Fig. 6. Two left panels: median Sérsic index as a function of stellar mass and normalized density distributions of the Sérsic index (n), respectively. Two right panels: median concentration (R_{90}/R_{50}) as a function of stellar mass and normalized density distributions of the concentration. The symbols of the medians are red filled circles for CLEs, orange open squares for RQEs, and blue stars for BSFs. The error bars correspond to the 16th and 84th percentiles. The distributions for CLE, RQE, and BSF galaxies are shown in red solid, orange open, and blue dashed histograms, respectively. The integral of each histogram sums to unity.

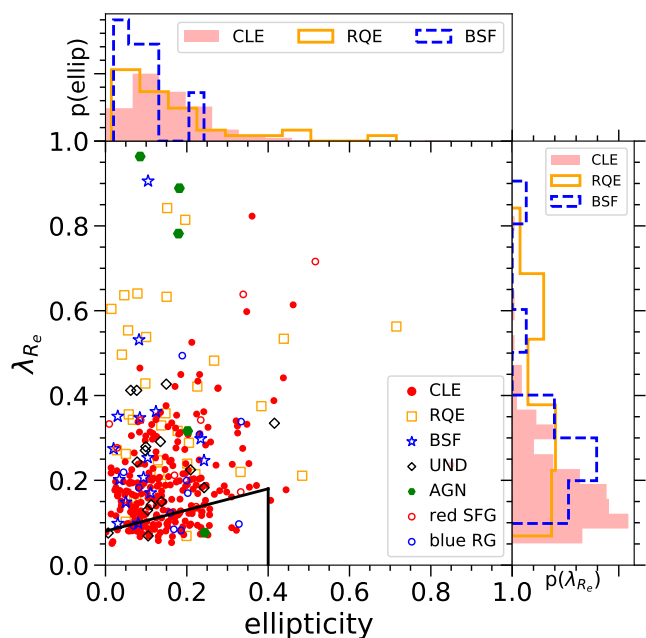


Fig. 7. Stellar spin parameter as a function of ellipticity. The symbols for the galaxies are the same as Fig. 1. The thick black lines enclose the non-regular rotators from Cappellari (2016). Top and right panels: normalized density distributions of ellipticity and λ_{R_e} , respectively, for CLE galaxies (red solid histogram), RQE galaxies (orange open histogram), and BSF galaxies (blue dashed histogram). The integral of each histogram sums to unity.

values of each stellar mass bin and radial bin. Then, we perform a linear fit for each resampled profile following the 2D version of the algorithm of Sheth & Bernardi (2012). This method allows us to obtain a distribution of the slopes for each “stacked” profile. The final gradient is the value that has the 50th percentile of this distribution (see Table 2). The reported errors of the gradients in the table are the standard deviations of their respective distributions. The gradients are in units of $\text{dex}/R_{\text{eff}}$ and are defined as:

$$\nabla \log(Y) = d \log(Y)/dR, \quad (3)$$

where Y is either age_{mw} , age_{lw} , Z_{mw} , or Z_{lw} , and R is the galactocentric radius in units of R_{eff} .

The ages and stellar metallicities per spaxel are calculated by weighting the respective SSP distributions by stellar mass or luminosity (e.g., Eqs. 1 and 2). We then use the weighted azimuthally-averaged profiles (using the stellar mass or flux maps) to obtain a profile that is not biased by local outliers (like very young regions) in a given radial region. For the sSFR radial profiles, we use the arithmetic azimuthal average for each radial bin. We calculate the standard deviation of each value per radial bin (we use this information to estimate the individual gradients below in Sect. 4.2). Figs. 8–10 show the “stacked” radial profiles with the median values and the 16th and 84th percentiles of our quantities for the five radial bins in three stellar mass bins.

Figure 8 shows the stacked (median) age_{lw} and age_{mw} radial profiles for CLEs, RQEs, and BSFs. It also shows the individual profiles of the RQE and BSF galaxies. We consider a lower mass limit of $M_{\star} = 10^{9.4} M_{\odot}$ in the lowest mass bin because there are only RQE galaxies at lower masses. By fitting a straight line to the stacked age profiles, the gradients in units of $\text{dex}/R_{\text{eff}}$ (see Eq. 3) can be calculated at each mass bin. Table 2 shows these gradients for the CLE, RQE, and BSF galaxies for each mass bin. The median age_{lw} is slightly older in the central part of the CLE population compared to their outskirts for all the masses. Similar behavior is seen in the case of RQEs with $M_{\star} < 10^{11} M_{\odot}$, although with overall younger age_{lw} than CLEs of the same mass (median age_{lw} between $10^{9.3}$ and $10^{9.7}$ yr for the former and $> 10^{9.7}$ yr for the latter) as expected by the selection criteria of the RQE galaxies. The massive RQEs show a different median trend, in which the central part is younger than the outskirts. The BSF population also shows a trend of slightly increasing age_{lw} with radius, although the profile is flatter on average at the $10^{10.4} < M_{\star}/M_{\odot} < 10^{11}$ mass bin. The age_{lw} values of BSFs are significantly younger than those of CLEs with the same mass at all the radii. Finally, the stacked age_{mw} profiles are flatter than the age_{lw} profiles, especially for the RQEs (see Table 2). The radial age_{mw} profiles of both RQEs and BSFs do not differ among them in a significant way.

In summary, the age_{lw} and age_{mw} stacked (median) profiles of the CLE galaxies show a mild decrease with radius at all mass bins, i.e., the central parts tend to be slightly older than the ex-

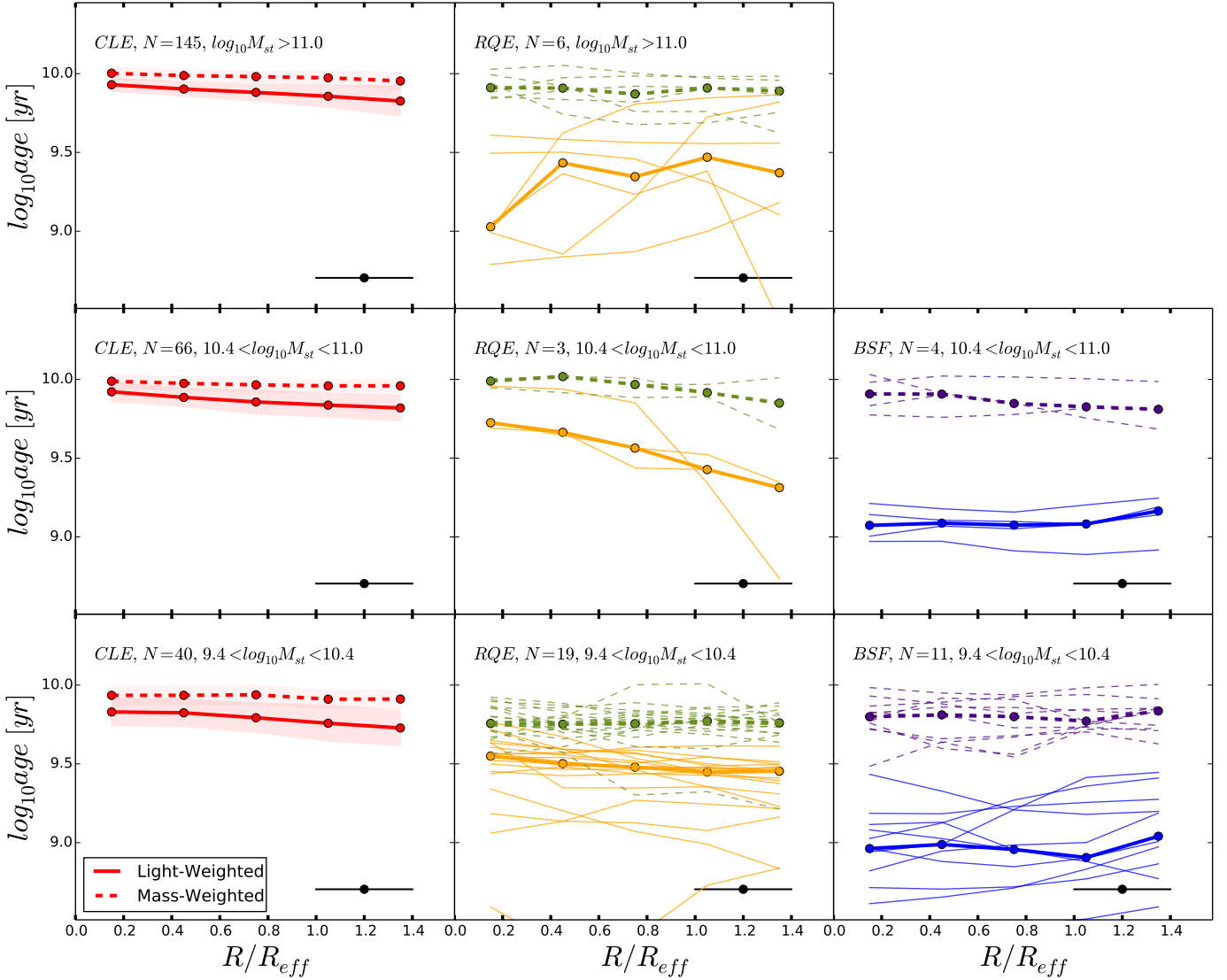


Fig. 8. Median mass-weighted and luminosity-weighted stellar ages profiles (dots connected with thick dashed and thick solid lines, respectively). The left column is for CLEs, the central column is for RQEs, and the right column is for BSFs. Each row is a stellar-mass bin, which increases from the bottom to the top. The shaded regions in the left panels correspond to the 16th and 84th percentiles (darker for the luminosity-weighted quantities). Given the relatively low numbers of RQE and BSF galaxies, we show the individual profiles as thin lines. The number of galaxies of each type in a given mass bin is shown in each panel. The horizontal error bar is the typical PSF size that represents the minimum radial resolution of the IFU.

ternal parts, which suggests a weak inside-out formation scenario for the CLE population. The age_{lw} radial profiles decrease slightly stronger than the age_{mw} ones, with average differences not larger than 0.2 dex. The age_{lw} and age_{mw} stacked profiles are more diverse for the RQEs and BSFs. In particular, the stacked age_{lw} profile of RQEs more massive than $10^{11} M_{\odot}$ tends to show a positive gradient, which could suggest an outside-in growth mode, although with large individual uncertainties. The big differences among the mass- and luminosity-weighted age profiles, which are typically larger than 0.2 dex (especially for the BSFs), show the presence of a relatively high fraction of young stellar populations in the BSF and RQE galaxies.

Figure 9 shows the stacked (median) luminosity- and mass-weighted stellar metallicity (Z_{lw} and Z_{mw} , respectively) profiles. The metallicity of CLEs is, on average higher for more massive galaxies, and it decreases with radius, steeper as more massive are the galaxies. We note the most massive CLEs tend to show some flattening in the Z_{lw} and Z_{mw} profiles at $R \gtrsim 1.0 R_{\text{eff}}$.

By fitting a straight line to the stacked profiles out to $1.5 R_{\text{eff}}$, the gradients in units of $\text{dex}/R_{\text{eff}}$ (see Eq. 3) can be calculated at each mass bin. Table 2 shows these gradients for both the luminosity- and mass-weighted stellar metallicities. Compared to the CLEs, the metallicity profiles are flatter for the RQEs, and the most massive RQE galaxies show even a positive gradient in both luminosity- and mass-weighted metallicities with large individual uncertainties, however. The BSF population tends to have a negative gradient, with the mass-weighted stacked profiles more pronounced than the luminosity-weighted ones at the two mass bins.

Finally, Fig. 10 shows the stacked (median) profiles of $\text{sSFR}(r) = \Sigma_{\text{SFR}}(r)/\Sigma_{*}(r)$, where the SFR is calculated in the last 30 Myr from the stellar population synthesis results. The sSFR shows how efficient the current SFR is with respect to the average in the past. It provides a criterion to evaluate whether a galaxy (or a galaxy region) is actively forming stars or it is quenching, or already it quenched. For example, it is common in

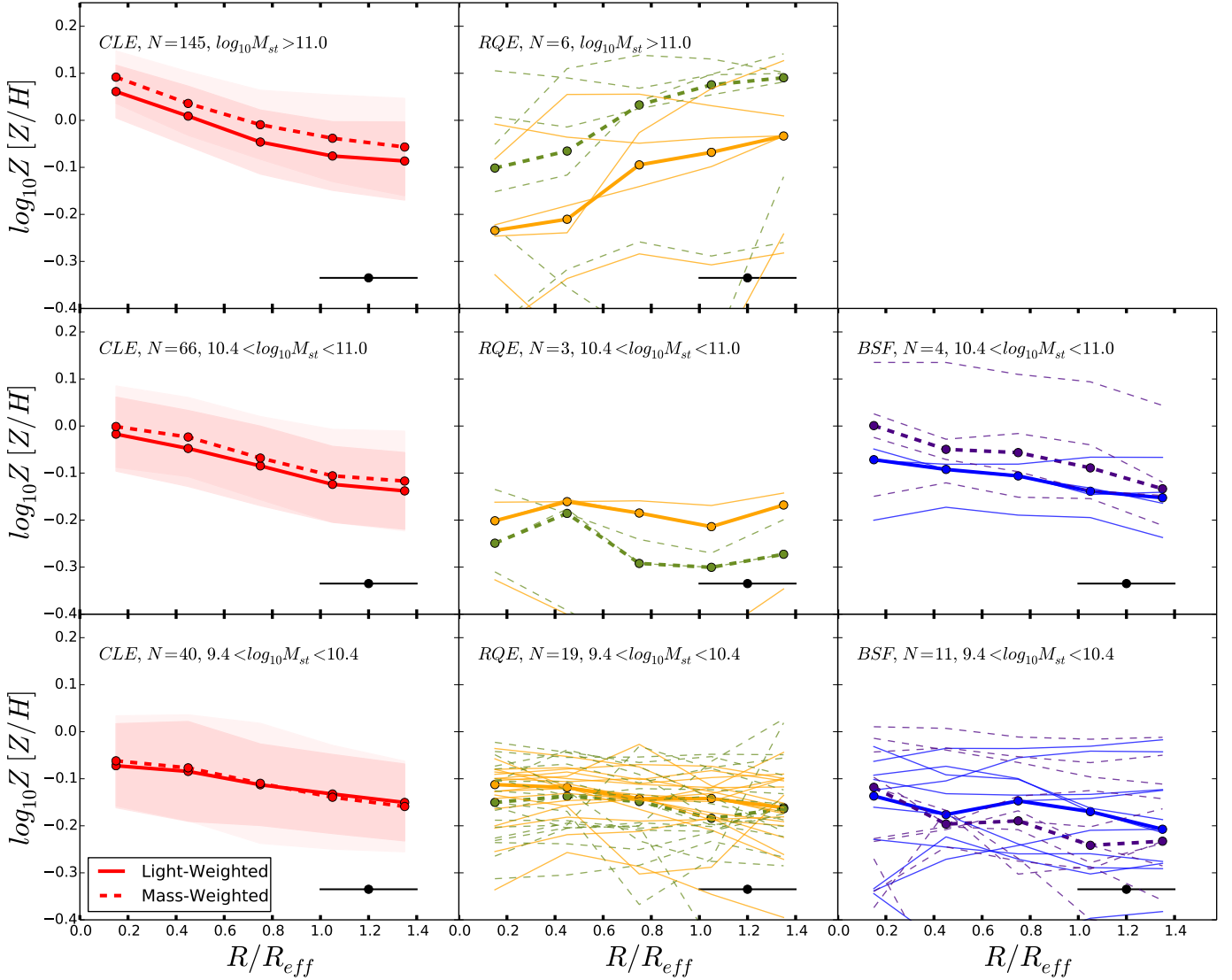


Fig. 9. Median mass-weighted and luminosity-weighted stellar metallicity profiles (dots connected with thick dashed and thick solid lines, respectively). The left column is for CLEs, the central column is for RQEs, and the right column is for BSFs. Each row is a stellar-mass bin, which increases from the bottom to the top. The shaded regions in the left panels correspond to the 16th and 84th percentiles (darker for the luminosity-weighted quantities). Given the relatively low numbers of RQE and BSF galaxies, we show the individual profiles as thin lines. The number of galaxies of each type in a given mass bin is shown in each panel. The horizontal error bar is the typical PSF size that represents the minimum radial resolution of the IFU.

the literature to define a galaxy as quenched or retired when its sSFR is lower than a critical value defined in between 10^{-11} and $10^{-10.7} \text{ yr}^{-1}$.

We find that the stacked sSFR profiles of low-mass CLE and RQE galaxies increase with radius, with the central part having values lower than the outer part by ~ 1 dex. This result suggests a more effective quenching process inside than outside (González Delgado et al. 2017; Belfiore et al. 2018; Ellison et al. 2018; Sánchez et al. 2018). For the higher mass bins, the median sSFR profile of the CLE population is roughly flat, though with a weak decrease toward the inner regions, suggesting a slightly more efficient quenching in these regions. For the massive RQE population, the sSFR profiles of most of the objects tend to be negative, suggesting an outside-in quenching. The BSFs exhibit higher values of sSFR at all the radii than CLEs and RQEs. In contrast to low- and intermediate-mass CLEs and RQEs, the sSFR profiles of BSF Es tend to be flat or slightly decrease with radius. We note the uncertainty in the constrained sSFR values below

10^{-12} yr^{-1} is large, so that these results for CLE galaxies should be taken with caution.

4.2. Individual stellar age and stellar metallicity gradients

We use the same methodology described in Sect. 4.1 but for the individual gradient values. We show in Figs. 11 and 12 individual gradients in stellar age and metallicity as functions of stellar mass. Table 3 presents the median values of the gradients and the 16th-84th percentiles for different mass bins and all the masses.

The CLE galaxies show mostly very mild negative or flat gradients in age_{mw} , whereas their gradients in age_{lw} are more negative. Only 19% and 8% of the CLE sample have positive gradients in age_{mw} and age_{lw} , respectively, confirming that the “stacked” age profiles in mass bins shown in Fig. 8 capture well the general behavior of the whole population. Also, in agreement with the “stacked” profiles, the individual metallicity gradients are more negative than the age gradients, and their scatter is also

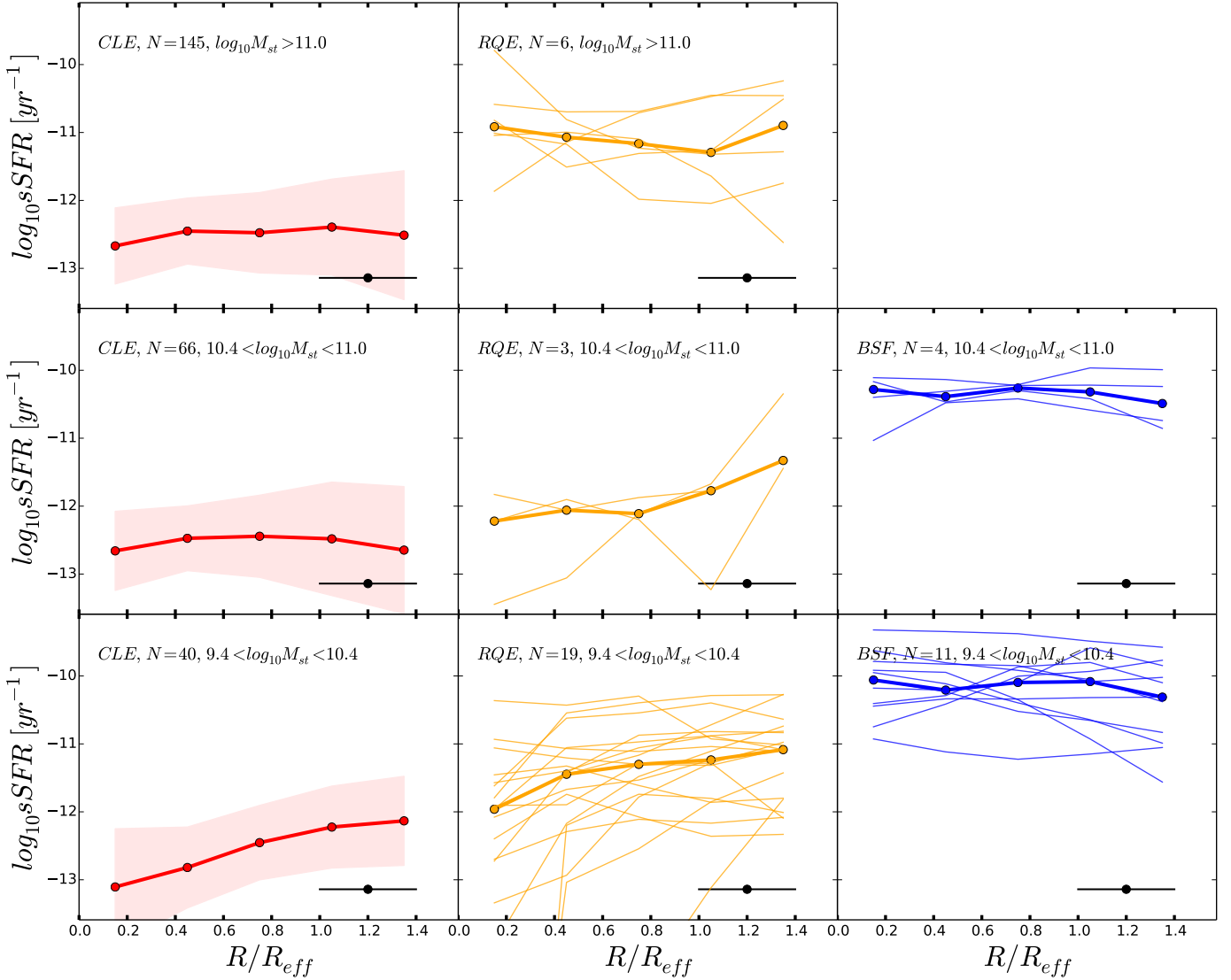


Fig. 10. Median sSFR profiles in the last 30 Myr obtained from the SFHs (dots connected with thick solid lines). The sSFR values below $\sim 10^{-12}$ yr^{-1} are very uncertain and can be considered upper limits. The left column is for CLEs, the central column is for RQEs, and the right column is for BSFs. Each row is a stellar-mass bin, which increases from the bottom to the top. The shaded regions in the left panels correspond to the 16th and 84th percentiles. Given the relatively low numbers of RQE and BSF galaxies, we show the individual profiles as thin lines. The number of galaxies of each type in a given mass bin is shown in each panel. The horizontal error bar is the typical PSF that represents the minimum radial resolution of the IFU.

Table 2. Gradients of the “stacked” profiles out to $1.5 R_{\text{eff}}$ in three stellar mass bins.

type	$\nabla \log$	$9.4 < \log(M_{\star}/M_{\odot}) < 10.4$	$10.4 \leq \log(M_{\star}/M_{\odot}) < 11$	$11 \leq \log(M_{\star}/M_{\odot}) < 12$
CLE	age_{lw}	-0.10 ± 0.06	-0.08 ± 0.05	-0.6 ± 0.05
CLE	age_{mw}	-0.01 ± 0.04	-0.02 ± 0.03	-0.03 ± 0.03
CLE	Z_{lw}	-0.08 ± 0.05	-0.12 ± 0.05	-0.11 ± 0.04
CLE	Z_{mw}	-0.11 ± 0.06	-0.11 ± 0.06	-0.13 ± 0.05
RQE	age_{lw}	-0.09 ± 0.13	-0.13 ± 0.02	0.26 ± 0.19
RQE	age_{mw}	-0.01 ± 0.05	-0.07 ± 0.02	-0.00 ± 0.06
RQE	Z_{lw}	-0.03 ± 0.03	0.04 ± 0.05	0.19 ± 0.10
RQE	Z_{mw}	-0.01 ± 0.06	-0.08 ± 0.06	0.18 ± 0.13
BSF	age_{lw}	0.10 ± 0.16	0.00 ± 0.05	
BSF	age_{mw}	-0.05 ± 0.06	-0.07 ± 0.06	
BSF	Z_{lw}	-0.02 ± 0.07	-0.06 ± 0.03	
BSF	Z_{mw}	-0.07 ± 0.08	-0.14 ± 0.05	

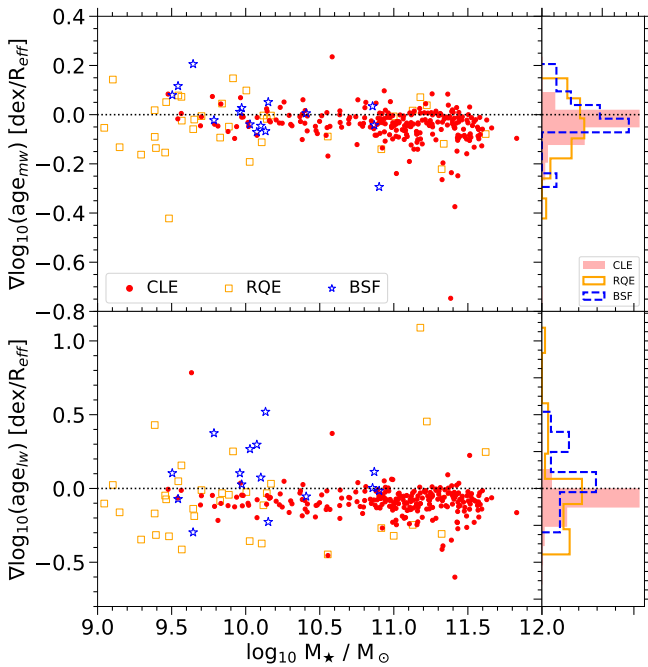


Fig. 11. Mass-weighted stellar age gradients (top-left panel) and luminosity-weighted stellar age gradients (bottom-left panel) as functions of the stellar mass of E galaxies. The symbols are red filled circles for CLEs, orange open squares for RQEs, and blue stars for BSFs. Top-right and bottom-right panels: normalized density distributions of mass-weighted age gradients and luminosity-weighted age gradients, respectively, for CLE galaxies (red solid histogram), RQE galaxies (orange open histogram), and BSF galaxies (blue dashed histogram). The integral of each histogram sums to unity. The dotted lines in the panels are gradients equal 0.

larger. For Z_{mw} and Z_{lw} , only 6% and 5% of the CLE sample show positive gradients, respectively. There is also a clear trend of steeper gradients as more massive are the galaxies, both for Z_{lw} and Z_{mw} . We will discuss the implications of these results in Sect. 6.2.

The RQE galaxies show evident larger scatters in their gradients compared to the CLEs. The medians of their mass- and light-weighted gradients tend to be mildly negative but the most massive bin ($M_* > 10^{11} M_\odot$), see Table 3. The gradients of age_{lw} , Z_{lw} , and Z_{mw} tend to be positive for massive RQEs. In the case of BSF galaxies, the scatter in age gradients is larger compared with that for CLEs, but the scatter in metallicity gradients is smaller or comparable between BSFs and CLEs. The median of the gradients in age and metallicity are slightly more positive than those of the CLEs of the same mass. We will discuss the implications of these results for RQEs and BSFs in Sects. 6.3.1 and 6.3.2, respectively.

We also explore the individual gradients of age_{mw} , age_{lw} , Z_{mw} , and Z_{lw} as functions of the integrated $g-i$ color, integrated mass-weighted and luminosity-weighted stellar ages, integrated mass-weighted and luminosity-weighted stellar metallicities, and λ_{R_e} . For the age_{mw} and age_{lw} gradients of CLEs, RQEs, and BSFs, we do not find any clear trend with the color, integrated galaxy ages and metallicities, and λ_{R_e} . We find mild dependences of the Z_{mw} and Z_{lw} gradients on the integrated luminosity-weighted age (more negative for older galaxies), and of the Z_{lw} gradients on both integrated metallicities (more negative for richer galaxies), and the $g-i$ color (more negative for redder galaxies). Since we find a dependence of the metallic-

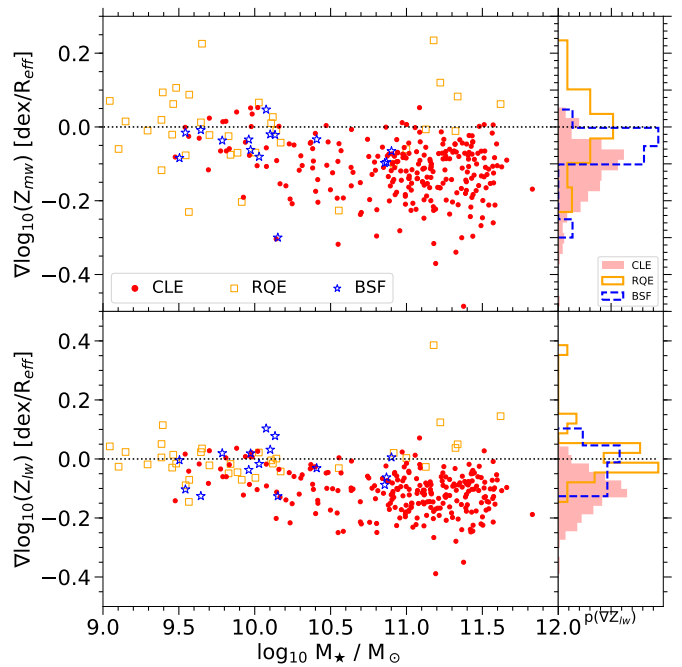


Fig. 12. Mass-weighted stellar metallicity gradients (top-left panel) and luminosity-weighted stellar metallicity gradients (bottom-left panel) as functions of the stellar mass of E galaxies. The symbols are red filled circles for CLEs, orange open squares for RQEs, and blue stars for BSFs. Top-right and bottom-right panels: normalized density distributions of mass-weighted metallicity gradients and luminosity-weighted metallicity gradients, respectively, for CLE galaxies (red solid histogram), RQE galaxies (orange open histogram), and BSF galaxies (blue dashed histogram). The integral of each histogram sums to unity. The dotted lines in the panels are gradients equal 0.

ity gradients on the stellar mass, these weak dependences of the metallicity gradients on the integrated stellar ages, metallicities, and color can be understood from the correlation between these physical parameters and the stellar mass (Figs. 2–5).

5. Stellar population age distributions

The fossil record method applied to the IFU data allows us to obtain not only mean spatially-resolved stellar population ages but the whole age distribution of the fitted SSPs integrated and within regions of the galaxies. With this information, it is possible to construct several temporal quantities, integrated and spatially resolved, that allow us to explore the evolution of galaxies. Examples of these quantities are the differential and cumulative SFHs, $SFR(t)$ and $SFR(< t) = \int_0^t SFR(t')dt'$, respectively; the birthrate parameter (Scalo 1986; Binney & Merrifield 1998),

$$b(t) \equiv \frac{SFR(t)}{\langle SFR(t) \rangle} = \frac{SFR(t)}{\frac{1}{t} \int_0^t SFR(t')dt'} \quad (4)$$

and the cumulative mass temporal distribution, CMTD,

$$M_*(< t) = \int_{t_1}^t SFR(t')[1 - R_{ml}(t')]dt', \quad (5)$$

where R_{ml} is the stellar mass-loss term. The CMTD is closely related to the cumulative SFH; the difference is that the stellar mass accumulated at each temporal step in the case of the CMTD takes into account the mass lost by stars as they evolve.

Table 3. Median mass- and luminosity-weighted gradients of stellar age and stellar metallicity out to $1.5 R_{eff}$ in units of dex/R_{eff} for different mass bins from Figs. 11 and 12. The last column is for the full mass range. The errors correspond to the 16th and 84th percentile range.

type	$\nabla \log$	$9.4 < \log(M_*/M_\odot) < 10.4$	$10.4 \leq \log(M_*/M_\odot) < 11$	$11 \leq \log(M_*/M_\odot) < 12$	$9 < \log(M_*/M_\odot) < 12$
CLE	age_{mw}	$-0.02^{+0.06}_{-0.03}$	$-0.03^{+0.04}_{-0.04}$	$-0.04^{+0.04}_{-0.06}$	$-0.03^{+0.04}_{-0.05}$
CLE	age_{lw}	$-0.08^{+0.06}_{-0.05}$	$-0.08^{+0.07}_{-0.05}$	$-0.08^{+0.05}_{-0.10}$	$-0.08^{+0.06}_{-0.07}$
CLE	Z_{mw}	$-0.06^{+0.07}_{-0.06}$	$-0.11^{+0.05}_{-0.08}$	$-0.12^{+0.06}_{-0.08}$	$-0.11^{+0.07}_{-0.08}$
CLE	Z_{lw}	$-0.05^{+0.06}_{-0.07}$	$-0.11^{+0.05}_{-0.08}$	$-0.12^{+0.06}_{-0.07}$	$-0.11^{+0.06}_{-0.07}$
RQE	age_{mw}	$-0.02^{+0.09}_{-0.10}$	$-0.09^{+0.06}_{-0.04}$	$-0.03^{+0.08}_{-0.11}$	$-0.02^{+0.09}_{-0.11}$
RQE	age_{lw}	$-0.05^{+0.08}_{-0.28}$	$-0.32^{+0.04}_{-0.09}$	$0.11^{+0.47}_{-0.37}$	$-0.08^{+0.19}_{-0.24}$
RQE	Z_{mw}	$-0.02^{+0.09}_{-0.05}$	$-0.10^{+0.03}_{-0.09}$	$0.07^{+0.07}_{-0.08}$	$-0.01^{+0.09}_{-0.07}$
RQE	Z_{lw}	$-0.02^{+0.04}_{-0.05}$	$0.00^{+0.01}_{-0.02}$	$0.09^{+0.11}_{-0.06}$	$0.00^{+0.05}_{-0.04}$
BSF	age_{mw}	$0.01^{+0.08}_{-0.07}$	$-0.02^{+0.04}_{-0.15}$		$0.01^{+0.07}_{-0.07}$
BSF	age_{lw}	$0.10^{+0.22}_{-0.24}$	$-0.01^{+0.07}_{-0.03}$		$0.07^{+0.22}_{-0.14}$
BSF	Z_{mw}	$-0.03^{+0.02}_{-0.05}$	$-0.08^{+0.03}_{-0.02}$		$-0.04^{+0.02}_{-0.06}$
BSF	Z_{lw}	$-0.00^{+0.05}_{-0.11}$	$-0.05^{+0.03}_{-0.03}$		$-0.02^{+0.05}_{-0.08}$

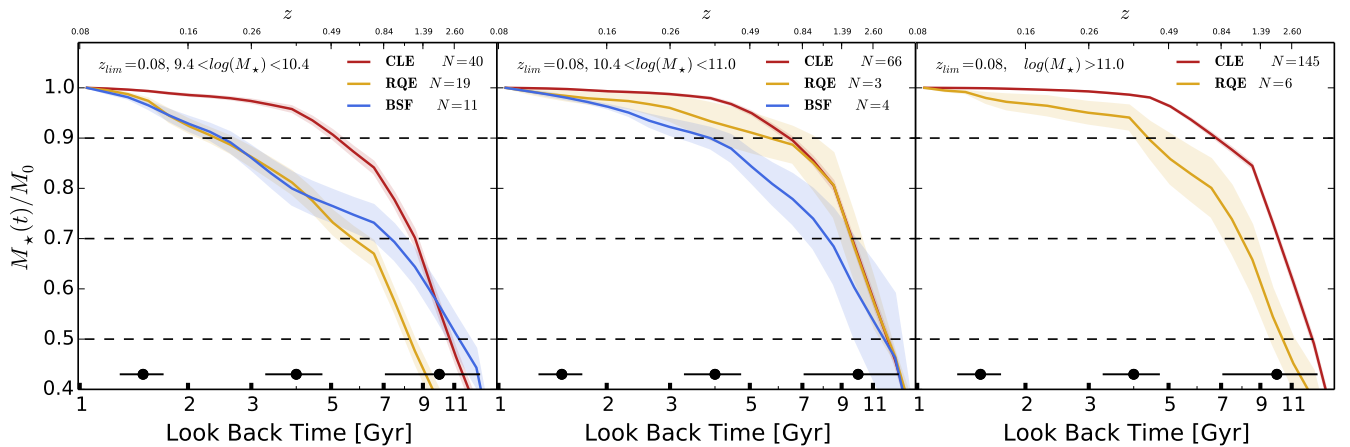


Fig. 13. Mean cumulative mass temporal distributions, CMTDs, within $1.5 R_{eff}$ in three stellar mass bins (mass increases to the right). The CMTDs are normalized to the mass attained at $z_{lim} = 0.08$. The red lines correspond to CLEs, the orange lines correspond to RQEs, and the blue lines correspond to BSFs. The shaded region is the error of the mean (standard deviation divided by \sqrt{N}) of the respective distribution. The number of galaxies of each type in a given mass bin is shown in each panel. The horizontal error bars show the average time resolutions of the SSP template stellar library.

5.1. Cumulative mass temporal distributions

Figure 13 shows the integrated (within $1.5 R_{eff}$) mean CMTDs normalized to M_0 for the CLE, RQE, and BSF galaxies in three stellar mass bins. The normalized CMTDs are constructed in the same way as reported in Ibarra-Medel et al. (2016; in that paper they were called normalized mass growth histories), where M_0 is the stellar mass attained at the same cosmological epoch for each galaxy. We define this epoch as the highest redshift of our sample, $z_{lim} = 0.08$ (look back time ~ 1 Gyr; in this way, we assure that all studied galaxies have their normalized CMTD determined at this time), i.e., M_0 is the stellar mass at $z = 0.08$. This mass is obtained by interpolating the CMTD around the time corresponding to $z = 0.08$. The normalized CMTDs can be interpreted as the speed at which the stellar mass grows at different epochs (Ibarra-Medel et al. 2016).

For all masses, the CLEs accumulated higher fractions of their final stellar masses (defined at $z = 0.08$) at earlier epochs on average, with higher mass growth rates in the past compared to RQEs and BSFs. At lower masses ($M_* < 10^{10.4} M_\odot$), the CLEs

accumulated 90% of their final mass ~ 5 Gyr ago, whereas it is between 2 and 3 Gyr ago for RQEs and BSFs. For masses $M_* > 10^{10.4} M_\odot$, the CLEs accumulated 90% of their mass ~ 7 Gyr ago, whereas it is between 4 and 6 Gyr ago for BSFs and RQEs. The mass growth of the CLEs tends to be earlier, with higher mass growth rates in the past, as more massive they are (downsizing). In contrast, the RQEs show a changing trend with mass. They accumulate on average the 90% of their mass at later epochs (~ 3 Gyr ago) at the lowest mass bin, later (~ 6 Gyr ago) at intermediate masses ($10^{10.4} < M_* < 10^{11} M_\odot$), and between 4 and 5 Gyr ago in the most massive bin. We note that the trends for RQEs with $M_* > 10^{10.4} M_\odot$ have large scatters. However, in general, the RQEs have a systematic delay in their normalized CMTDs compared with the CLEs, as seen in Fig. 13. The BSFs also present a clear delay in their CMTDs with respect to the CLEs. These results are consistent with the younger mean ages for the RQEs and BSFs with respect to the CLEs reported in Sect. 3.

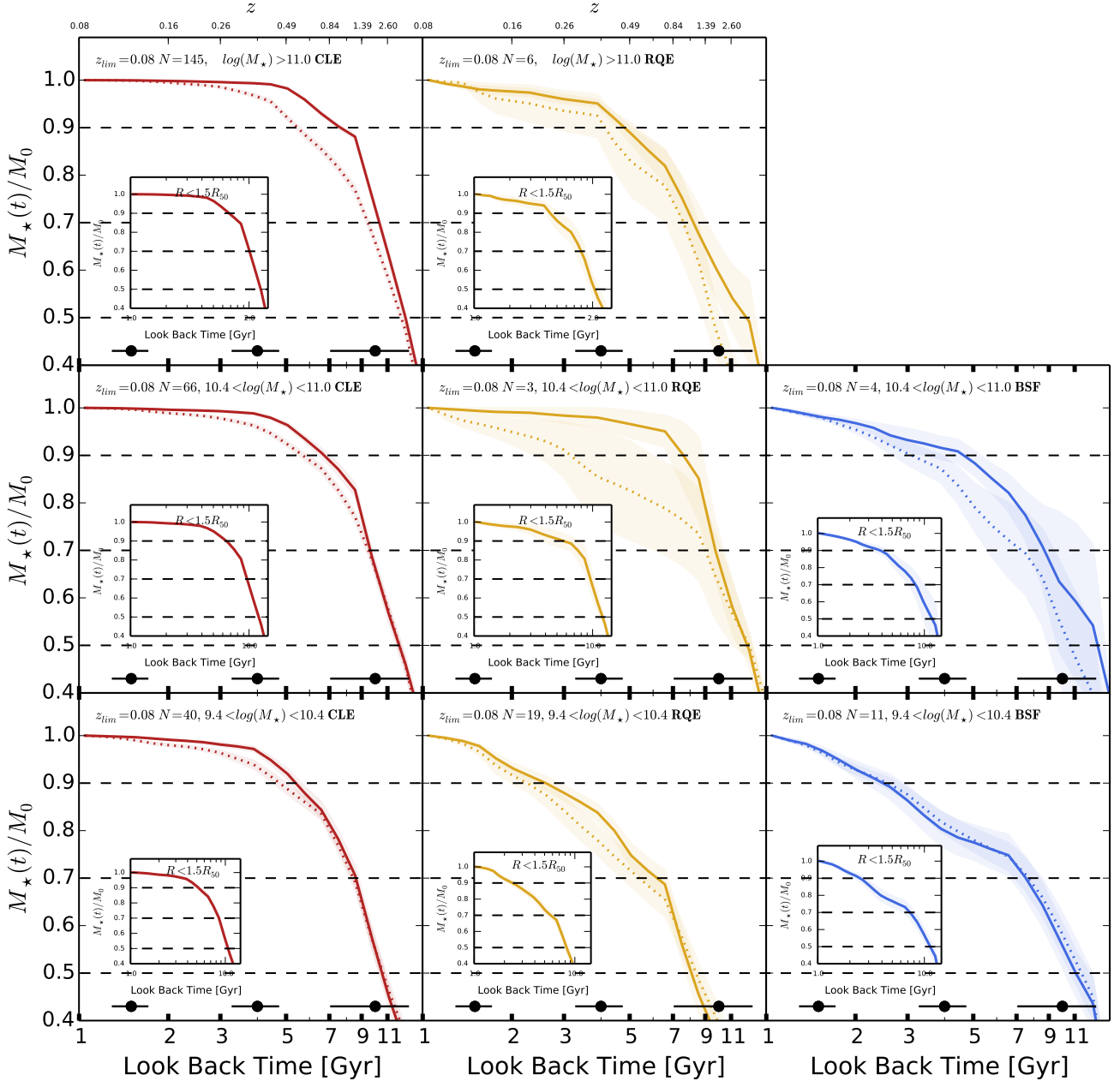


Fig. 14. Mean cumulative mass temporal distributions, CMTDs, for each E type in three mass bins. Each row is a stellar-mass bin, which increases from the bottom to the top. The CMTDs are normalized to the respective masses at $z_{lim} = 0.08$. The left column is for CLEs, the central column is for RQEs, and the right column is for BSFs. In each panel, the solid line corresponds to the mean CMTD within $0.5 R_{eff}$, whereas the dotted line corresponds to the mean CMTD between 1 and $1.5 R_{eff}$. The light and dark shaded regions are the errors of the mean (standard deviation divided by \sqrt{N}) of the distributions in the inner part and the outer part of the galaxies, respectively. The horizontal error bars show the average time resolution of the SSP template stellar library at the given epoch. The inset box shows the integrated mean normalized CMTDs within $1.5 R_{eff}$.

Figure 14 shows the mean normalized CMTDs for CLEs, RQEs, and BSFs in two radial bins; the inner part of the galaxies ($R < 0.5 R_{eff}$, solid lines) and the external part of the galaxies ($1.0 < R/R_{eff} < 1.5$, dotted lines). In this case, M_0 is the mass attained within each one of these two radial bins at $z = 0.08$. The results are shown for the same three mass bins as in previous figures. The CLEs typically present a weak inside-out growth mode; their inner stellar mass growth rates were slightly higher in the past than the outer ones, and as a result, the inner part ac-

cumulated 90% of its mass at earlier times than the outer part. This trend is more evident for the more massive CLEs. We notice, however, that the inside-out growth mode is much more pronounced for late-type galaxies (see, e.g., González Delgado et al. 2015; Ibarra-Medel et al. 2016; García-Benito et al. 2017; Avila-Reese et al. 2018; López Fernández et al. 2018). The RQEs show less clear and more scattered trends with mass. The inside-out growth mode seems to occur in RQEs galaxies, but it is much weaker and noisier for the most massive ones, $M_* > 10^{11} M_\odot$.

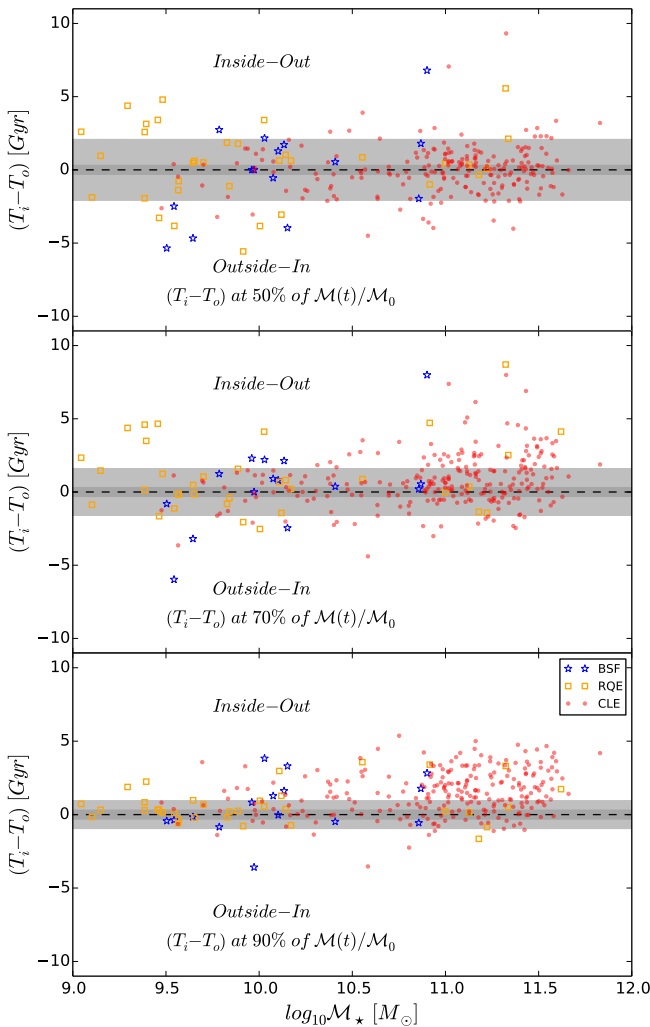


Fig. 15. Difference of look-back times between the internal part ($R < 0.5 R_{\text{eff}}$) and the external part ($1 < R < 1.5 R_{\text{eff}}$), $(T_i - T_o)$, when each accumulates 50%, 70%, and 90% of the mass (from top to bottom panels) as functions of the total stellar mass. The red dots, orange squares, and blue stars correspond to CLE, RQE, and BSF galaxies, respectively. Above (below) the dashed lines, the E galaxies would be assembled inside-out (outside-in). The shaded regions correspond to the temporal resolution allowed by the SSP template library at the earliest ages of the galaxies in each panel.

This different behavior in the CMTDs for massive RQEs is an agreement with the “stacked” age and metallicity radial profiles presented in Sect. 4 for the RQEs in the same mass bin. Regarding the BSFs, their average inner and outer normalized CMTDs are statistically similar, suggesting this either a radial homogeneous stellar mass assembly or strong radial mixing processes. The more massive BSFs show more explicit evidence of an inside-out mode. However, given the small numbers of RQEs and BSFs, the mean trends showed in Fig. 14 should be taken with caution since they can be dominated by the extreme behavior of a few galaxies (see below).

We notice that the differences in mean normalized CMTDs of the external and inner parts of a given E galaxy can be smaller than the age resolution of the used SSP libraries for ages corresponding to look-back times higher than ~ 8 Gyr⁶. Fig. 15

shows this comparison. Here we plot for each galaxy the difference between the look back times of the normalized CMTDs corresponding to the internal and the external parts, $(T_i - T_o)$, when each attains 50%, 70%, and 90% of the mass in the corresponding radial bin as functions of the galaxy M_\star . When $(T_i - T_o)$ is larger (smaller) than 0, we have formally the inside-out (outside-in) growth mode. However, when $|T_i - T_o|$ is smaller than the uncertainty in the age determination, we can not conclude anything more than that the radial growth mode is roughly uniform within this age uncertainty. The light grey bands in Fig. 15 show our rough estimates of the age resolution allowed by the fossil record method at the different mass fractions, which correspond on average to different epochs. The radial mass growth of CLEs passes from roughly homogeneous at epochs when they accumulated $\sim 50\%$ of their inner and outer masses (within the age uncertainty of the fossil record method) to clearly inside-out mass growth mode when they accumulated 90% of their inner and outer masses, i.e., the inside-out mode becomes relevant at later epochs of the mass growth. The (late) inside-out mode tends to be stronger for more massive CLEs in all the panels. The RQE galaxies do not show systematic differences with M_\star in the mass growth between the internal and external parts. Most intermediate- and low-mass RQEs show some evidence of inside-out growth mode though weaker than the CLEs. In the case of the massive RQEs, two (1/3) of them show evidence of an outside-in mode at least since times where 70% of their inner and outer parts have formed, while other two massive RQEs show clear inside-out growth mode. The BSFs show a large scatter in this figure, though not too different from the CLEs of similar masses.

5.2. Specific star formation histories

Figure 16 shows the mean integrated (within $1.5 R_{\text{eff}}$) specific SFHs for CLEs, RQEs, and BSF Es in three stellar-mass bins⁷. They are normalized to their values attained at $z_{\text{lim}} = 0.08$. The mean specific SFHs of CLEs show a sharp decrease with time, faster as more massive are the galaxies. This behavior is likely associated with quenching processes rather than natural aging due to gas consumption; see more details below. For the RQEs, their mean specific SFHs are roughly similar to those of the CLEs at the largest look back times, but then they decrease slower. In particular, the mean specific SFHs of the RQEs remain roughly constant since ~ 5 to 2 Gyr ago for masses $M_\star < 10^{11} M_\odot$ and since ~ 2.5 to 1.5 Gyr ago for larger masses, and then decrease fast. This result implies that the progenitors of the RQEs at these epochs were more efficient in growing their stellar mass by SF than the CLEs, and only recently suffered significant decline in SF. The specific SFHs of the BSFs show behavior similar to the RQEs but without sharply decreasing lately as the RQEs.

Figure 17 shows the mean specific SFHs for CLEs, RQEs, and BSFs in two radial regions and three stellar mass bins. Similar to Fig. 14, the inner part of the galaxies ($R < 0.5 R_{\text{eff}}$) and the external part of the galaxies ($1.0 < R < 1.5 R_{\text{eff}}$) are shown in solid and dotted lines, respectively. The inner mean specific

them in such a way that the exact age determination of them is very uncertain. For example, the fossil record method applied to MaNGA IFU data with a reasonable signal-to-noise ratio (S/N) recovers the ages of stellar populations older than 10 Gyr with uncertainty not better than $\pm(2.5 - 3)$ Gyr. Estimates of the uncertainty in age determination with the fossil record method at different stellar population ages are shown in Figs. 13 and 14 as the horizontal error bars.

⁷ We smoothed the specific SFHs by a step filter with a width of 32 Myr to minimize the impact of numerical spikes.

⁶ As discussed in Ibarra-Medel et al. (2016; 2019; see the references therein), the spectra of old stellar populations are very similar among

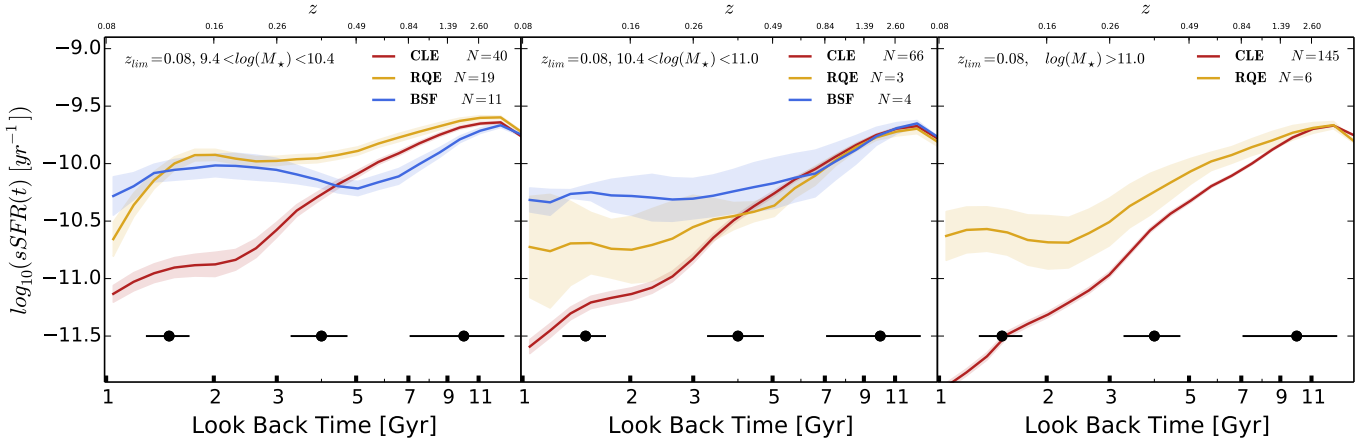


Fig. 16. Integrated mean specific SFRs as functions of look back time, i.e., integrated mean sSFHs, within $1.5 R_{\text{eff}}$ in three stellar mass bins (mass increases to the right). The sSFHs are normalized at $z_{\text{lim}} = 0.08$. The red lines correspond to CLEs, the orange lines correspond to RQEs, and the blue lines correspond to BSFs. The shaded region is the error of the mean of each sSFR. The number of galaxies of each type in a given mass bin is shown in each panel. The horizontal error bars show the average time resolution of the SSP template stellar library at the given epoch.

SFHs of the CLEs decrease faster than the outer ones, suggesting that CLEs suffer inside-out quenching, more pronounced for the more massive ones. In the case of the low-mass RQE and BSF galaxies, the inner and outer mean specific SFHs show relatively constant SFHs since 5 Gyr down to the present for the BSFs and down to ~ 2 Gyr ago for the RQEs. The BSFs of intermediate masses also show constant radial SFHs down to the present. At the same mass, the inner part of the RQEs shows a rapid decrease of the sSFR to lower redshifts, whereas the specific SFH of the outer parts is still constant. The most massive RQEs show slight evidence of outside-in quenching, with the outer parts starting to significantly decline their SF faster ~ 4 Gyr ago, on average, than the inner parts.

5.3. Epoch and time-scale of long-term quenching in SF

In the literature there is not a common and exact definition of SF long-term quenching in galaxies; see for some recent discussions, e.g., Schawinski et al. (2014); Smethurst et al. (2015); Pacifici et al. (2016); Carnall et al. (2018). As consume their gas reservoir, galaxies decrease their SFRs according to their internal metabolism, even the star-forming ones, which likely accrete gas by cosmological infall during long periods of their lives. Let us call this cycle of decreasing gas accretion and its consumption into stars due to the internal metabolism of galaxies nominally as aging. In a general way, by quenching, one understands a decline in the SFR significantly faster than normal aging, produced by some internal or external mechanisms. These mechanisms may deprive galaxies of gas infall, promote its ejection from the galaxy, or avoid the cold gas to be transformed into stars (for some reviews of different quenching mechanics, see, e.g., Ibarra-Medel et al. 2016; Smethurst et al. 2017; and more references therein). The different quenching mechanisms have different time scales of SF cessation.

We have mentioned above that the sSFR histories of CLEs show a pronounced decline. We would like now to evaluate how fast happens this decline of SF for our sample of MaNGA E galaxies. We anticipate that it is beyond the scope of this paper to explore possible processes and mechanisms of quenching. A first step for estimating the time-scale of quenching is to determine the epoch at which a given galaxy becomes long-term quenched. Several approaches are used in the literature to define the long-

term quenching time, t_q , of galaxies. For example, t_q is defined as the cosmic time when the sSFR decreased below a given factor f times the inverse of the Hubble time (e.g., Firmani & Avila-Reese 2010; Pacifici et al. 2016) or when the birthrate parameter b decreased below a given factor f' (Carnall et al. 2018). Both factors are related, given that $\text{sSFR}(t) \approx b(t)/[(1 - R_{\text{ml}})t]$; the approximation is because it is assumed R_{ml} independent of time, which is roughly correct after ~ 2 Gyr of evolution for a given SSP. A second step is to define a characteristic time of maximal SFR from which the galaxy started to decline, on average, its SFR, t_{max} . For galaxies with several stages of increase and decrease of the SFR, there is not an unambiguous time of maximum SFR. Operationally, we relate here t_{max} to the luminosity-weighted average age of the galaxy, age_{lw} ⁸, considering it as an average epoch at which the galaxy had still active star formation. The time difference $\Delta t_q = t_q - t_{\text{max}}$ is then the quenching time-scale.

To define the long-term quenching time t_q from the criterion $b(t) = f'$, we use the last of the times when this criterion is attained. For our sample of E galaxies, we have experimented with values of f' from 0.8 down to 0.1. For high values, there are galaxies for which Δt_q is negative, and many of our BSF Es appear as quenched. For low values of f' , the quenching time of some Es, mainly RQEs, is not attained and the Δt_q values of most of the Es are too large. We have found that $f' = 0.4$ is an optimal value because all of our BSF Es are confirmed as not retired galaxies, and only a few RQEs do not attain the criterion of quenching.

Figure 18 shows the quenching look back times, $t_{\text{q,LB}}$, and quenching time-scales, Δt_q , calculated from the (non-parametric) stellar population age distributions of each one of our MaNGA E galaxies; red circles are for CLEs and orange squares for RQEs. The upper and right panels show the normalized histograms of $t_{\text{q,LB}}$ and Δt_q , respectively. CLEs quench on average 3.8 ± 1.2 Gyr ago and not earlier than 7.3 Gyr ago ($z \approx 1$). For values of f' lower than 0.4, the quenching look back

⁸ We pass from age to look back time adding to age_{lw} the observation time of each galaxy, and from look back time to cosmic time using the Universe age of 13.67 Gyr for the cosmology assumed here.

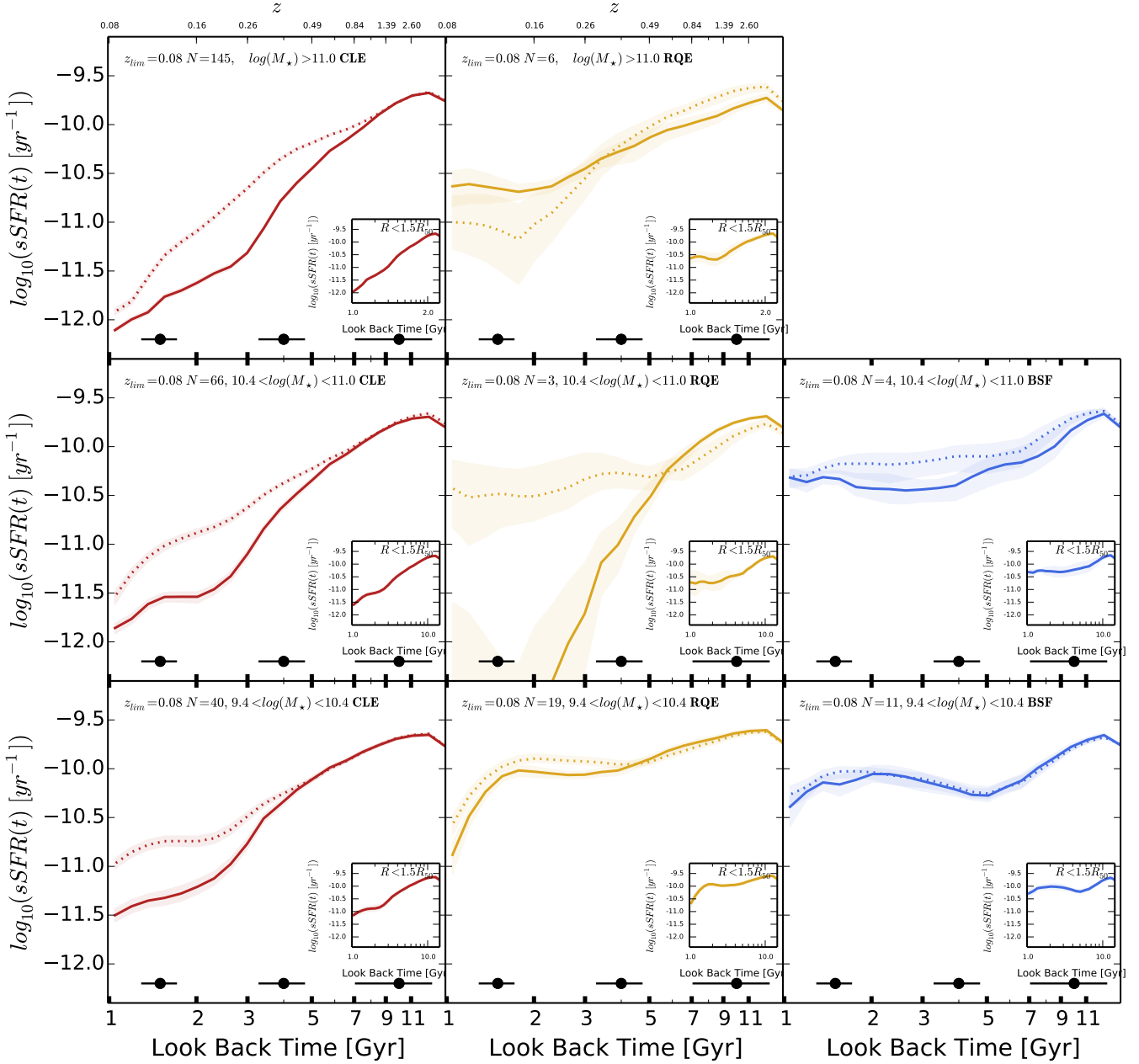


Fig. 17. Mean sSFHs for each E type in three mass bins, which increases from the bottom to the top. The left column is for CLEs, the central column is for RQEs, and the right column is for BSFs. In each panel, the solid line corresponds to the mean sSFR within $0.5 R_{\text{eff}}$, whereas the dotted line corresponds to the mean sSFR between 1.0 and $1.5 R_{\text{eff}}$. The light shaded region and dark shaded region are the errors of the mean of the sSFRs in the inner part and the outer part of the galaxies, respectively. The horizontal error bars show the average time resolution of the SSP template stellar library at the given epoch. The inset box shows the integrated mean specific SFHs within $1.5 R_{\text{eff}}$.

times result even later (lower redshifts)⁹. The RQEs, as expected, quench later than the CLEs, 1.2 ± 0.9 Gyr ago on average.

⁹ The emergence of a quenched population of galaxies could result too late from our archaeological analysis compared to observations from cosmological surveys, which show a non-negligible fraction of passive or quenched galaxies at $z \sim 2$ (see, e.g., Muzzin et al. 2013; Whitaker et al. 2013; Pandya et al. 2017). However, we note that: (i) Our galaxies may have several epochs of quenching (and SF increasing), but we define the long-term quenching time as the last of these epochs; therefore, one expects some fraction of our galaxies to be counted as quenched several times at epochs earlier than the assigned t_q . (ii) For accurate comparisons and to overcome the progenitor bias, it is important to use

Regarding the long-term quenching time-scale Δt_q , the CLEs take 3.4 ± 0.8 Gyr to quench on average, while RQEs quench faster, in 2.4 ± 0.5 Gyr on average. For the CLE population, we find some anticorrelation between Δt_q and $t_{\text{q,LB}}$: as earlier is the long-term quenching, faster it happens; for those CLEs that quenched ~ 7 Gyr ago, $\Delta t_q = 1\text{--}1.5$ Gyr. In contrast, RQEs

large volume-complete samples, and to use similar criteria in the fossil record and high redshift samples to define quenching times and galaxy quenched populations. The study of both questions mentioned above is beyond the scope of this paper.

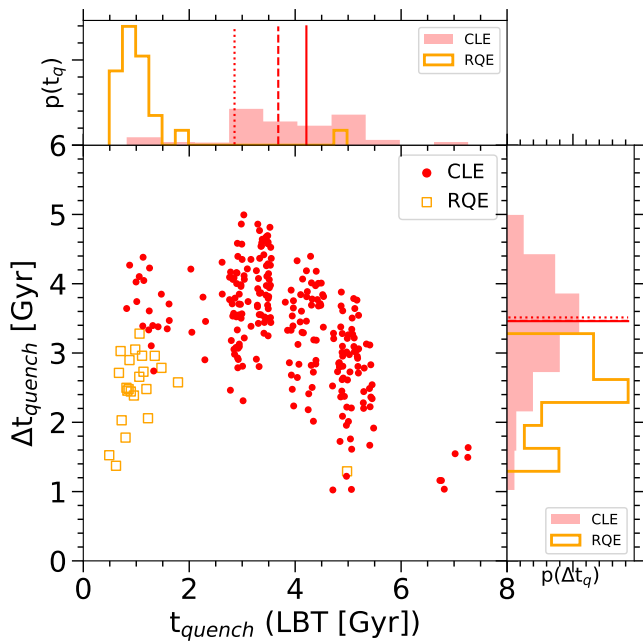


Fig. 18. Long-term quenching look back time ($t_{q,LB}$) and quenching time-scale (Δt_q) calculated from the non-parametric stellar population age distributions (see Sect. 5.3 for details). Red circles are for CLEs and orange squares are for RQEs. The upper and right panels show the normalized distributions of $t_{q,LB}$ and Δt_q , respectively, for CLE galaxies (red solid histogram) and RQE galaxies (orange open histogram). The integral of each histogram sums to unity. The vertical (horizontal) lines in the upper (right) panel correspond to median values of $t_{q,LB}$ (Δt_q) for CLE galaxies in three stellar mass bins: $9.4 < \log(M_\star/M_\odot) < 10.4$ (dotted), $10.4 \leq \log(M_\star/M_\odot) < 11$ (dashed), and $11 \leq \log(M_\star/M_\odot) < 12$ (solid).

quench late and relatively fast, occupying a different region than CLEs in the Δt_q – $t_{q,LB}$ plane; this provides one more evidence that the RQEs significantly segregate from the dominant population of CLEs. For the latter, there is a trend of $t_{q,LB}$ with M_\star in the sense that more massive galaxies quench earlier. In the histograms of Fig. 18, the median values of $t_{q,LB}$ and Δt_q corresponding to the low-, intermediate-, and high-mass bins used along this paper are indicated with the dotted, dashed, and solid lines, respectively.

We also calculate the normalized long-term quenching time-scale, $\eta_q \equiv \Delta t_q/t_{\max}$, which measures the galaxy quenching duration as a fraction of the age of the Universe when the quenching started, that is, when the galaxy was by last time yet actively forming stars (recall that we approximate this cosmic time as the corresponding to the luminosity-weighted age of the given galaxy). For CLEs, on average, $\eta_q = 0.50 \pm 0.15$, that is, these galaxies quenched roughly half the time they attained their most active SF phase. For RQEs, $\eta_q = 0.23 \pm 0.06$. This result could be interpreted as a high quenching efficiency, but it could also be related to the efficiency of a possible post-merging quenching process rather than the quenching of an individual galaxy, in which case it is not easy to interpret η_q for them.

A typical function used to describe the SFH of galaxies is the so-called τ -delayed model:

$$\text{SFR}(t) = \frac{A(t - t_i)}{\tau^2} \exp \frac{t - t_i}{\tau}, \quad (6)$$

where t_i is the onset time of SF, and $A[M_\odot]$ is a normalization factor. The SFR grows linearly after t_i , it attains a maxi-

mum at $t_{\max} = t_i + \tau$, and then it decreases exponentially. In López Fernández et al. (2018), the authors used several parametric SFHs for their stellar population synthesis inversion models applied to the IFS observations from the CALIFA survey (Sánchez et al. 2012). For the τ -delayed function and in the case of their E galaxy sample, they report look-back initial times of $t_{i,LB} = 10.1 \pm 5.1$ Gyr and $\tau = 1.4 \pm 1.4$. For the τ -delayed function, we can define the long-term quenching time-scale as $\Delta t_q = t_q - t_{\max}$. By using our definition of t_q as the time when $b(t) = 0.4$, we find that Δt_q strongly depends on τ and weakly on t_i , $\Delta t_q \approx (0.15t_i + 2.46)\tau + 0.02t_i + 0.37$. For the range of values of $t_i = 3.35 \pm 0.5$ Gyr constrained in López Fernández et al. (2018) for E galaxies, and for $\tau = 1.4$ Gyr, $\Delta t_q \approx 4.5$ –4.7 Gyr. These values are ~ 1 Gyr larger than the average $\Delta t_q = 3.4$ Gyr value found here for CLEs. The SFHs of individual galaxies are diverse, and in many cases, the τ -delayed function does not describe them well. Despite this and the many differences between López Fernández et al. (2018) and our fossil record method, it is encouraging that the differences in the obtained typical values of Δt_q for E galaxies are not large. Finally, we notice that when approaching the SFHs to the τ -delayed model, values of $\tau \sim 1$ Gyr imply long-term quenching times-scales (using our definition of t_q , when $b = 0.4$) of 3.0–3.4 Gyr for reasonable t_i values of 1–4 Gyr, respectively.

6. Discussion

In this section, we discuss the caveats of our methodology (Sect. 6.1), and summarize and discuss the interpretations of the results presented in the previous sections. The CLEs are the main population of E galaxies, and our large sample allows us to claim for generic evolutionary trends for them (Sect. 6.2). This could not be the case for the RQE and BSF samples due to the diversity of their properties and evolutionary features, and the low numbers. In any case, we propose and discuss in Sect. 6.3 some possible generic evolutionary trends for them.

6.1. Caveats of the methodology

Pipe3D uses a brute-force minimization that explores all possible parameters that will achieve the best linear combination of the SSP stellar libraries, which best fits the observed spectrum. At the same time, Pipe3D performs a Gaussian fitting of the observed emission lines (Sánchez et al. 2016b;a). The inversion methods, in general, have an intrinsic precision limit in determining the ages of the stellar populations that compose the spectrum (therefore, in the recovered SFH or CMTD) due to the degeneracy of spectral features with age, especially for old populations; see Sánchez et al. (2016b) and Ibarra-Medel et al. (2016) for an extensive discussion on this question, and more references therein. According to these papers, the average logarithmic age uncertainty of Pipe3D is around 0.1–0.15 dex. This uncertainty drives the peaks of the SFH to spread out and lower their amplitudes, with consequences also in the shape of the inferred normalized CMTDs. Besides the age resolution effects, systematical uncertainties in the results from the inversion method are introduced by the SSP and dust extinction models and the choice of the IMF. Sánchez et al. (2016b) and Ibarra-Medel et al. (2016) discussed extensively on the expected effects of these ingredients on the SFHs and CMTDs (there called mass growth histories).

Ibarra-Medel et al. (2019) directly explored how well the integral and radial SFHs and CMTDs are recovered with Pipe3D, including the effects of galactic extinction and observational settings like the S/N, IFU spatial resolution, and galaxy inclination.

They used post-processed state-of-the-art hydrodynamical cosmological simulations of well-resolved late-type and early-type galaxies. Regarding the inversion method, they found that the precision in the inferred SFHs (and CMTDs and sSFHs), as expected, decreases as older is the stellar age of the “observed” stellar populations: the inversion method tends to smooth more and more the real SFHs for ages older than 5 Gyr. This effect diminishes the original inside-out trend at the radial level, especially for the late-type galaxies, which present a more complex SFH and a more prominent inside-out mode than the early-type ones. Nevertheless, Pipe3D still manages to recover the qualitative behavior of the real radial SFHs and CMTDs at early epochs; the recovery is much more precise at late epochs. The main reason for these issues in recovering the SFHs is the limited age sampling of the used SSPs as the ages are older (Sánchez et al. 2016a; Ibarra-Medel et al. 2019). For that reason, in this paper we used the Pipe3D age sampling resolution of the SSPs as a rough indicator of uncertainty of the inversion method in the recovery of the real SFHs or CMTDs at different epochs (horizontal error bars in the Figs. 13–14 and 16–17).

Ibarra-Medel et al. (2019) also tested the ability of the fossil record method to recover the age and metallicity radial profiles of the mock galaxies analyzed under the observational settings of MaNGA. They found that the mass- and luminosity-weighted profiles tend to be flattened by the fossil record method, particularly for late-type galaxies as more inclined they are and when the IFU spatial resolution is poor. They noted that young populations, even if their fraction in mass is small, ‘contaminate’ significantly the given spectrum so that the inversion method tends to overestimate the fraction of these populations, with the consequent recovery of younger ages and lower stellar masses than the true ones. When young populations are present, the effects of this contamination affect more the radial bins that contain intrinsically larger fractions of old populations, that is, the innermost ones, assigning them lower ages and metallicities, which lowers the gradients. Ibarra-Medel et al. (2019) warn against overinterpreting the age and metallicity gradients of galaxies with poorly sampled IFS data and high inclinations. For early-type galaxies, especially the CLEs, the mentioned above effects are much less severe than for late-type galaxies.

6.2. The CLE galaxies

6.2.1. Radial gradients: comparisons with previous works and implications

There are different radial mass growth modes of early-type galaxies discussed in the literature based on their calculated stellar age radial profiles. Most of the reported luminosity-weighted age slopes for E+S0 galaxies are distributed within the $[+0.1, -0.1]$ interval¹⁰, i.e., around 0 (e.g., Sánchez-Blázquez et al. 2007, Reda et al. 2007, Spolaor et al. 2010, Rawle et al. 2008; 2010 with VIMOS IFU; Kuntschner et al. 2010 with SAURON; Boardman et al. 2017 with Mitchell Spectrograph IFU; Goddard et al. 2017 with MaNGA; San Roman et al. 2018 with the ALHAMBRA survey, see more references therein), and also for only E galaxies (Koleva et al. 2011 with long-slit data and Martín-Navarro et al. 2018 with CALIFA).

The median mass- and luminosity-weighted age gradients we have found here for CLEs are $-0.03^{+0.04}_{-0.05}$ and $-0.08^{+0.06}_{-0.07}$

dex/ R_{eff} , respectively, which suggest a weak inside-out formation. Among those works close to our one, Goddard et al. (2017) find that the mass-weighted median age gradients tend to be slightly positive for E+S0 galaxies in MaNGA, which suggests a weak outside-in formation. Domínguez Sánchez et al. (2019) find negative light-weighted age gradients for E galaxies in MaNGA, but the most massive galaxies show mildly positive age gradients. They find the age gradients are weaker if there are IMF gradients as well. Using the CALIFA survey, Zibetti et al. (2020) reported mildly positive luminosity-weighted age gradients for E+S0 galaxies, tough in the inner regions ($\lesssim 0.4 R_{eff}$), the profiles tend to be U-shaped. In contrast, González Delgado et al. (2015) find mildly negative light-weighted mean age gradients for E galaxies in CALIFA, and Zheng et al. (2017) find mildly negative mass-weighted mean age gradients for Es in MaNGA, which are consistent with an inside-out formation scenario. Parikh et al. (2019) also report mildly negative age gradients for E+S0 galaxies in MaNGA, but Li et al. (2018) and Ferreras et al. (2019) find mildly positive age gradients for low-mass E+S0 galaxies in MaNGA and SAMI, respectively.

Different observational settings, spectral fitting codes, stellar population models, and methods to derive the stellar age gradients may explain the diversity of results discussed above. In Appendix A we show examples of the luminosity- and mass-weighted age profiles for individual MaNGA galaxies shown in Goddard et al. (2017; see their Fig. 7). Our luminosity-weighted age profiles are consistent with those of Goddard et al. (2017). However, our mass-weighted age profiles are also mildly negative or flat, which is opposite to the positive mass-weighted age gradients reported by them. At this point, it is difficult to make conclusive statements about the formation scenarios of early-type galaxies based only on the stellar age profiles given the mixed results in the literature using different approaches. Fortunately, more information can be obtained from the spatially-resolved IFS observations. Note also that our study is particularly unique with respect to previous ones because we focus (i) only on morphologically well-defined E galaxies (S0 are not taken into account), and (ii) only on “red and dead” E galaxies (CLEs), separating those E galaxies with evidence of recent quenching, blue colors, or ongoing star formation.

For the metallicity radial profiles, the results in the literature agree that the vast majority of early-type galaxies present negative gradients. However, the different works do not agree in how steep these negative gradients are (see for recent reviews San Roman et al. 2018; Zibetti et al. 2020). The shallow slopes we find for our sample of CLE galaxies (see Tables 2 and 3) are consistent with most of recent works based on studies of large galaxy samples (e.g., González Delgado et al. 2015; Wilkinson et al. 2017; Goddard et al. 2017; Zheng et al. 2017; San Roman et al. 2018; Li et al. 2018). Gas-rich dissipative collapse models (Larson 1974) including SN-driven winds (e.g., Pipino et al. 2010) or their revised versions in the hierarchical clustering cosmological scenario (e.g., Cook et al. 2016; Taylor & Kobayashi 2017), predict steep negative gradients in metallicity after the dissipative phase. The steepness of the gradients can result lower by low SF efficiencies induced by SF feedback (Pipino et al. 2008; 2010) in less massive galaxies or by non-dissipative (dry) mergers (Kobayashi 2004; Di Matteo et al. 2009; Hirschmann et al. 2015; Cook et al. 2016; Taylor & Kobayashi 2017) in more massive galaxies, at least externally. If the mergers are gas-rich, central SF can regenerate the gradients (Hopkins et al. 2009), though the efficiency of this process is limited by processes that can suddenly quench SF. The final metallicity gradients depend on all of

¹⁰ In some papers the gradient slopes are calculated per dex in age and per dex in physical radial units (kpc), and in other ones in per dex in age and in units of R_{eff} . The reported slopes are then in units of dex/dex or dex/ R_{eff} , respectively.

these processes and the fractions of stellar mass formed or assembled in the different phases.

Regarding the dependence of the metallicity gradient on mass, previous observational results disagree among them (see for a review Oyarzún et al. 2019). We find that the gradient slopes tend to become flattened as less massive the CLEs are, which agrees with the proposal that SN-driven winds lower the SF efficiency in galaxies with weaker gravitational potentials. On the other hand, for the more massive CLEs, while the inner gradients remain relatively steep, at radii larger than $\sim 1 R_{\text{eff}}$ the metallicity profiles tend to flatten (see the top-left panel of Fig. 9), which agrees with the proposal of posterior dry mergers. The latter result is consistent with Oyarzún et al. (2019), who also found that the stellar metallicity profiles of massive E+S0 MaNGA galaxies fall with radius but flatten externally. In conclusion, we find negative metallicity gradients with relatively shallow slopes, which support the scenario of early gas-rich dissipative collapse for CLEs combined with mass-dependent processes that tend to lower the steepness of the gradients.

As Oyarzún et al. (2019) extensively discuss, some of the apparent differences in the measured metallicity gradients of early-type galaxies among many observational works may be due to the used definition of metallicity gradients, as well as due to the different metallicity tracers or stellar population fitting codes employed to calculate the stellar metallicity. We add to this discussion that differences may also arise from the way the samples of early-type galaxies are selected. Our work is probably more accurate in this sense since it refers exclusively to red, quenched, and morphologically classified pure E galaxies.

Finally, we find that the radial sSFR profiles decrease on average toward the center, suggesting inside-out quenching. Indeed, the average radial specific SFHs show that the quenching on average is faster in the inner part compared to the external one, see Fig. 17. In the case of the CLEs less massive than $10^{10.4} M_{\odot}$, some residual SF would be needed to maintain the sSFR relatively flat in the external parts during the last 2 or 3 Gyr. The inside-out quenching can be produced: by an early central compaction process that triggers bursts of SF with the consequent gas consumption and gas ejection by SN-driven feedback, leaving not too much gas for further SF (this process also would help to reduce the negative metallicity gradient; Dekel & Burkert 2014; Tacchella et al. 2016; Avila-Reese et al. 2018); by the AGN feedback (e.g., Bluck et al. 2016; 2020; Guo et al. 2019); by morphological quenching, that is, when the formed dynamically hot spheroid stabilizes the inner gaseous disk avoiding further SF (e.g., Martig et al. 2009); or by a combination of the previous mechanisms over time (Lin et al. 2019).

6.2.2. A two-phase formation scenario

From the archaeological study of our well-defined morphological sample of 251 CLE galaxies, we find that they accumulated 70% of their current stellar masses 8–11 Gyr ago with an evident “downsizing” trend, especially in that regards the formation of their last 10–20% mass fraction. As discussed above, the CLEs show mostly mild negative or zero light- and mass-weighted age gradients, and relatively steep negative gradients in both light- and mass-weighted metallicities. Besides, the mass- and luminosity-weighted ages do not differ too much among them both for the integrated ages and for the ages along the galacto-centric radius. At earlier epochs, the inner and outer parts of CLEs formed their stellar populations roughly homogeneously, while at later epochs the outer parts tend to form later than the inner ones, especially for the more massive galaxies.

On the other hand, the inner parts tend to decrease their specific SFRs faster than the outer parts. All these results suggest that the CLEs formed a significant fraction of their stars early (> 8 Gyr) and nearly coeval in time and radius, followed by an inside-out growth and a quenching process that also proceeded the inside out. These trends become stronger as more massive are the galaxies.

From the archaeological analysis of the CLEs, we have estimated that they finished their quenching globally (retired) on average 3.8 ± 1.2 Gyr ago and not earlier than 7.3 Gyr ago, with quenching time-scales (from a typical epoch of active SF to the long-term quenching time) of 3.4 ± 0.8 Gyr on average. Besides, though with a large scatter, the trend is that CLEs that retired earlier did it faster. A possible explanation of this trend could be that CLEs generally form early by intense bursts of SF, followed by a rapid decline of SF. However, many of them can continue growing in stellar mass lately by (dry) accretion of other galaxies, whose stellar populations can be younger, i.e., these galaxies were forming stars after the central one already retired. The archaeological analysis of a galaxy assembled this way will show a later epoch of SF quenching and a larger quenching time-scale than the early formed primary galaxy. An analysis of long-term quenching times and time-scales in the inner and outer regions of the CLEs, and separating galaxies into centrals and satellites, may help explore this question of two-phase E galaxy formation. Such a study will be presented elsewhere.

In a general way, the results reported here for CLEs are consistent with prediction from hydrodynamic simulations of the formation of spheroid-dominated galaxies (e.g., Naab et al. 2009; Oser et al. 2010; Navarro-González et al. 2013; Rodriguez-Gomez et al. 2016; Rosito et al. 2018; 2019a;b). These simulations show that massive spheroid-dominated galaxies follow, in general, a two-phase formation scenario, which consists of an initial gas-rich (dissipational) collapse onto dark matter halos, where the bulk of the stellar mass is formed, and a late dry accretion of satellites and eventual (dry) major merger events. The consistency between our results and those of simulations is evident even in some specific details. For example, according to Rosito et al. (2019a), for values of $\lambda_{R_e} = 0.17$, which is the median measured in our CLEs, the stellar mass-weighted ages should be older than 8 Gyr. This is consistent with the overall old stellar populations of our CLE galaxies from the age_{mw} distribution (see Fig. 4).

6.3. The RQE and BSF galaxies

Following, we discuss the nature and evolution of the RQE and BSF galaxies. These two samples are about 15% out of our whole sample of E galaxies and are characterized mainly by showing evidence of late events of SF. This is in line with Thomas et al. (2010), who from a SDSS sub-sample of early-type galaxies, have reported that $\sim 10\%$ of them present young ages (< 2.5 Gyr), being they more frequent at lower masses and lower-density environments. They interpreted these early-type galaxies as the result of rejuvenation processes (see also Shapiro et al. 2010). We caution that our attempt to find general evolutionary trends for the RQE and BSF samples is flawed by low numbers as well as for the possibility that these galaxies rather than homogeneous subpopulations, are just objects that deviate from the main trends due to peculiar and diverse evolutionary conditions. In forthcoming papers, we will present an individual spectroscopic analysis of each RQE and BSF galaxy, including kinematics, as well as detailed photometric and environmental analysis. This detailed analysis will allow us to confirm or mod-

ify the generic interpretations we propose here tentatively for RQEs and BSF galaxies.

6.3.1. RQE galaxies

Do RQEs, as defined here, have different properties and evolutionary paths with respect to CLEs? Our results suggest that, indeed, this is the case, reassuring that our selection criteria were able to pick a class of physically different E objects. The RQEs are significantly younger than the CLEs on average, even at a given M_\star , see Fig. 4; the differences are on average by ~ 5 Gyr using age_{lw} as expected given the selection criterion with age_{lw} , and by 3–4 Gyr using age_{mw} . At low masses of $9.4 < \log(M_\star/M_\odot) < 10$, the RQEs are younger than CLEs with on average differences of $age_{mw} \sim 2$ Gyr. The gradients in age_{mw} of the RQEs are on average flat but there is a large scatter around 0, see Fig. 11. The gradients in age_{lw} are even more scattered and clearly differ between RQE galaxies more and less massive than $\sim 10^{11} M_\odot$; for the former, the gradients tend to be positive while for the latter, they tend to be negative (see Fig. 11, and Tables 2 and 3). We recovered 71% of the RQEs within the empirical region of the urz diagram that can capture the youngest portion of quiescent blue elliptical galaxies according to McIntosh et al. (2014; see Fig. 3). In fact, only 2% of the CLEs are contained inside this region. At low masses of $9.4 < \log(M_\star/M_\odot) < 10$, we recover 92% of the RQE galaxies, whereas 28% of the CLEs are located within this region. Furthermore, the progenitor(s) of RQEs were most of the time in an active phase of SF (at least one of them if they suffered a late merger), opposite to the progenitor of CLEs, see Fig. 16. Finally, the RQEs of all masses not only quenched recently ($t_q = 1.2 \pm 0.9$ Gyr ago) but notably faster than the CLEs, even comparing to those CLEs that also have late long-term quenching times (see Fig. 18). For instance, low-mass RQE galaxies show a median $t_q \sim 1$ Gyr and $\Delta t_q = 2.5$ Gyr, whereas those are 2.9 Gyr and 3.5 Gyr, respectively, for CLE galaxies of the same mass. All these facts suggest that RQEs are not a simple statistical extension of the properties of CLEs, including the low-mass range in which they overlap, and may support the distinction of RQEs and CLEs as two different classes of E galaxies. The definition of RQE galaxies is strongly motivated by McIntosh et al. (2014), but we admit it is sort of arbitrary, and the numbers reported above might change with other definitions to classify them. There exists the possibility that the RQE galaxies actually correspond to a continuous transition of CLE galaxies at low masses, in which the boundary is not totally clear.

The luminosity-weighted ages of RQEs are significantly lower than the mass-weighted ones at all masses. However, while for RQEs with $M_\star < 10^{11} M_\odot$ the difference increases outward, for most of the more massive ones, it increases inward (see Fig. 8). A difference with mass is also seen in the stellar metallicity gradients; both the mass- and luminosity-weighted gradients are nearly constant or slightly negative for most of the less massive RQEs, while both gradients are positive for most of the massive galaxies. Moreover, for the massive RQEs, Z_{lw} is significantly lower than Z_{mw} , while for the less massive RQEs, Z_{lw} is slightly higher than Z_{mw} (see Fig. 5). The latter also have younger stellar populations outward, with metallicities higher than those of the dominant old populations, while for the massive RQEs, the younger populations tend to dominate in the central regions. Interestingly enough, the specific SFHs of the less massive RQEs show evidence of very weak inside-out quenching. Instead, for the massive RQEs, on average the SF in external regions seems to have quenched faster than in the inner regions (outside-in

quenching). All these results suggest that RQEs more massive than $\sim 10^{11} M_\odot$ differ on their radial stellar populations from the less massive ones.

Why the RQE galaxies quenched so late and fast? Were they early-type galaxies before that, or is the morphological transformation what triggered their quenching? Do they assemble by late mergers? Following, we discuss on these questions separately for the RQEs less and more massive than $\sim 10^{11} M_\odot$. Our discussion is based on the archaeological results presented above. By construction, from the archaeological approach, it is not possible to infer the dynamical assembly history of galaxies (mergers). However, some consequences of the dynamical assembly may leave imprinted in the global and radial properties of their stellar populations, helping us constrain scenarios that imply mergers. The discussed scenarios are highly speculative and are based on the reported generic trends of only a few objects, so they should be considered just as proposals to be confirmed with more detailed object-by-object studies.

RQEs less massive than $10^{11} M_\odot$: A simple scenario, where the RQEs defined here are the tail of delayed evolution of CLEs is not enough to explain several of the differences mentioned above, particularly the different slopes of RQEs in their specific SFHs compared to CLEs of similar masses. Based on our results, we can speculate that most of the RQEs suffered a relatively late, intermediate (1:3 to 1:8 mass ratio) merger, where at least one of the merging galaxies was star-forming and gas-rich (the less massive one, which has been accreted presumably by an earlier-type galaxy). This gas-rich late merger scenario (or the rejuvenation scenario in some cases, see below) may explain why the specific SFH of these RQEs, which can correspond to at least two galaxies in the past, is relatively high and nearly constant until ~ 2 Gyr ago.

From Fig. 16 one sees that the mean specific SFHs of RQEs decrease relatively fast, similar to those of the CLEs, but at some time the former, instead of keeping decreasing, become roughly constant. This time can be indicative of the SF activity of the gas-rich secondary when the primary progenitor entered already in its quenching phase. The stellar mass fractions formed at these times account on average for $\sim 60\%$ and 90% of the final masses of the low- and intermediate-mass RQEs, respectively. Therefore, since then ($z < 0.8$), the RQE main progenitors could have experienced accretion of a gas-rich satellite (or simply of gas), which comprise between 40% and 10% of their final mass, respectively. Before and during the late gas-rich event, the interaction enhances the SF (starburst), consuming this gas; the accreted gas can also activate a (weak) AGN. Indeed, gas-rich mergers have been suggested as a mechanism that triggers the shut-down of SF in quenched galaxies at $z \sim 0.8$ (Wu et al. 2020). If a disk remains yet, since the system becomes strongly spheroid dominated, it likely becomes stable against disk instabilities (morphological quenching; Martig et al. 2009), which also quenches the SF. As a result, it is likely that a fraction of the young stellar populations forms from more enriched gas than the old populations belonging to the more massive, earlier-type progenitor, so their metallicities are expected to be higher than those of the older stellar populations (see lower panel of Fig. 5). From a preliminary analysis of fine morphological structures (Appendix C), we find a high incidence of broad tides in the RQEs of masses above $\sim 10^{10} M_\odot$; the broad tides (fans and plumes) are fossils of intermediate or major mergers that took place not too long ago (e.g., Mancillas et al. 2019; and more references therein). In a lower fraction of the RQEs have also seen shells.

In addition to the gas-rich late merger scenario, for some low-mass ($M_\star \lesssim 10^{10} M_\odot$) RQE galaxies, a process of gas infalling from the cosmic web (typically of low metallicity) or gas that was acquired through internal stellar mass loss may have produced a “rejuvenation” of SF that stopped recently. Assuming the BSFs galaxies are well described by “rejuvenation” of their SF (see below), and given the similarities between the RQE and BSF galaxies of the low-mass bin in the metallicity profiles and the radial specific SFHs, this scenario is plausible for some RQE galaxies. We also note that the incidence of fine structures strongly decreases for the low-mass RQEs (Appendix C), although this could be partially due to effects of surface brightness sensitivity given the low luminosities of these galaxies.

RQEs more massive than $10^{11} M_\odot$: For these galaxies¹¹, or for some of them, the results discussed above can be consistent with the presence of a late ($z < 0.3$ –0.5), intermediate or major merger of a primary early-type progenitor with a secondary gas-poor galaxy but with younger populations on average than the primary. Most of the accreted smaller galaxy is expected to fall by dynamical friction to the center of the larger, older one. This scenario may explain why the stellar populations in the inner parts of the final RQE show evidence of younger ages, lower metallicities, higher sSFRs, and later onset of quenching than in the outer parts. According to this scenario, most of the inner populations of the local RQE formed actually in the accreted satellite, which formed later and had more sustained SF activity than the primary early-type galaxy. On the other hand, in contrast to the less massive RQEs, the merger for these RQEs could be dry because as more massive are the galaxies, they are poorer in gas content.

The kinematics of the massive RQEs seems to support our gas-poor late merger scenario. For them, the median values of $(\epsilon, \lambda_{R_e})$ are (0.19, 0.35), while for massive CLEs these values are (0.14, 0.14). Thus, the median values of the massive RQEs lie well outside the region of non-regular rotators (see Fig. 7). Their values of λ_{R_e} and galaxy mass fit within the class D described by Naab et al. (2014), which corresponds to galaxies that experienced, in addition to minor mergers, a recent ($z < 1$) collisionless major merger leading to a moderate rotation. The median structural parameters (Sérsic index and concentration) tend to be similar between massive CLEs and RQEs (see Fig. 6), although with larger scatter for lower values, i.e., more disky structures, in the case of the RQEs. From our preliminary morphological analysis of fine structures (Appendix C), we find that 85% of the massive RQEs present broad tides, evidencing this the occurrence of a recent, intermediate or major merger.

Finally, the massive RQEs are, in general, above the line that separates blue and red galaxies (see Fig. 2). The median g - i colors also tend to be similar between massive CLEs and RQEs, although slightly redder for the former than the latter (1.29 and 1.26, respectively). Therefore, they do not seem to currently belong to a green valley population of galaxies at these masses.

To confirm the generic (and highly speculative) scenarios proposed above for RQEs, or to favor other possibilities, we will study the IFS information of each RQE individually elsewhere, including kinematics, their morphological features from deep optical images, and their environments.

¹¹ The MaNGA IDs (and Plate-IFU designs) of these galaxies are 1-152806 (manga-8936-6101), 1-44063 (manga-8718-6101), 1-594755 (manga-8612-1901), 1-604860 (manga-8714-3704), 1-633196 (manga-8485-12703), and 1-634238 (manga-7992-12701).

6.3.2. The particular case of the BSF galaxies

The BSFs are younger at all radii on average than RQEs and CLEs, especially when using age_{lw} . The BSFs tend to have also lower metallicities. The large differences between the ages or metallicities weighted by mass and those weighted by luminosity (Figs. 4–5 and 8–9) show that the BSF ellipticals suffered very recent episodes of SF. The gradients in both age_{mw} and age_{lw} are nearly flat, but the gradients in age_{lw} for low-mass BSFs tend to be positive. The gradients in Z_{mw} and Z_{lw} are flatter than those of the CLEs of the same mass, and some times even positive. We note that there are not very massive BSFs (they have $M_\star < 10^{11} M_\odot$). These results are consistent with the inferred mean CMTDs, which show that BSFs accumulated most of their stellar masses later than CLEs regardless of the mass. The radial age_{mw} profiles and CMTDs of BSFs show evidence of inside-out growth, suggesting they acquired their E morphology similar to the CLE galaxies. The main difference is when they accumulated most of their stellar masses. The BSFs accumulated 90% of their total mass late, between 2 and 4 Gyr ago on average. The integrated specific SFHs show that the BSFs had an early quenching phase similar to their CLEs counterparts, but then while the CLEs suffered a long-term quenching, the BSFs have continued forming stars at relatively high rates (Fig. 16). The departure between the BSFs and CLEs starts on average 4 (5) Gyr ago for low-mass (intermediate-mass) galaxies. At the moment of the departures in the sSFR, CLEs and BSFs had assembled more than 90% and 80% of their total mass, respectively. These results suggest BSFs experienced accretion events at $z < 0.5$ that triggered SF and comprised around 20% of the final mass in these E galaxies. Such late events are not frequent in CLEs.

Are the BSF galaxies a sample of intermediate- and low-mass CLEs rejuvenated by recent gas accretion or gas-rich (wet) minor mergers? Or are they post-starburst galaxies with recent morphological transformation? Are they located in particular environments?

As mentioned above, our results suggest the BSF galaxies evolve initially similarly as the CLE galaxies of the same mass, but they formed a fraction of their stars later, and are still forming stars, following a rejuvenation. Regarding the environment, Lacerna et al. (2016) did not find BSF Es in dense environments such as the Coma supercluster. Lacerna et al. (2018) found that isolated BSF Es are not located in dense large-scale environments compared with other isolated E galaxies using different proxies to define the environment within 5 Mpc. Therefore, the rejuvenation process of E galaxies seems to occur only in low or average density environments. However, these environments do not ensure the E galaxies would be blue and star-forming in general; most of the isolated E galaxies in low-density environments actually show red colors with very low SFRs¹² (Lacerna et al. 2016; 2018). Finally, from the preliminary fine-structure morphological analysis presented in Appendix C, we find that $\sim 30\%$ of the BSF Es present broad tides (as less massive are the BSFs, less frequent are the broad tides), that is, only less than a third of the BSFs show evidence of late mergers. The incidence of shells is slightly larger; shells are long-lived fine structures product of mergers that could have taken place several Gyr ago (e.g., Mancillas et al. 2019).

¹² Morphological quenching (Martig et al. 2009), compaction (Tacchella et al. 2016), type-Ia Supernovae feedback, and AGN feedback (Yesuf et al. 2014; Lacerna et al. 2018) can be mechanisms to shutdown SF in most of the intermediate- and low-mass E galaxies that live in average or low-density environments, where the environmental and halo quenching are not suitable.

We propose that BSF Es formed as E quiescent galaxies of similar masses but suffered late accretion of low-metallicity gas from the cosmic web or from a minor merger with a gas-rich galaxy that can sustain their SF for 4–5 Gyr at least. In some cases, the renewed SF can be even due to gas acquired through internal stellar mass loss (Shapiro et al. 2010). The rejuvenation acts before galaxies are long-term quenched. The scenario of rejuvenation for BSF Es explains the following general results: i) their age_{mw} are younger on average than those of the CLEs and much younger in the case of age_{lw} , evidence of late bursts of star formation; ii) their stellar metallicities are similar or slightly lower than those of the CLEs, but with a larger dispersion, which shows a fraction of the stellar population in the BSFs formed on average from gas with less enrichment than the CLEs and with a large scatter in the level of enrichment; iii) their specific SFHs are roughly continuous in the last 4–5 Gyr, that is, they present a sustained late activity of SF, though at earlier epochs they were quenching similar to their CLE counterparts; and iv) their Z_{mw} and Z_{lw} gradients are flatter than those of the CLEs, especially for Z_{lw} , which means their younger stellar populations were formed from gas with roughly equal metallicity in the central and external parts of the galaxy. In the rejuvenation scenario by gas accretion from the cosmic web or minor gas-rich mergers, likely an inner disk forms within the E galaxy, and SF proceeds within it, probably in a low efficient regime due to the spheroid that stabilizes the gaseous disk avoiding the efficient formation of molecular clouds. Interesting enough, the BSF Es present roughly flat sSFR radial profiles (Fig. 10), similar to what is observed in disk star-forming galaxies (e.g., Sánchez et al. 2018) but with lower amplitudes. These results are in line with those reported by Shapiro et al. (2010), who showed that the SF in early-type galaxies is a scaled-down version of similar processes in more vigorously star-forming galaxies.

A key signature of the rejuvenation scenario is the presence of an inner star-forming disk within the BSF Es. From the morphological and kinematics analysis presented in Appendix C, we find that almost all the BSFs show a disky star-forming central structure, some times kinematically decoupled. The SF in inner disk components has been suggested as a mechanism that contributes to the rejuvenation of the stellar populations in the central regions, which may explain the outside-in formation history found in low-mass spheroidal dominated galaxies (bulge-to-total mass ratios > 0.5), in the EAGLE simulation (Rosito et al. 2019b). However, our results show that the inside-out formation is still present in E galaxies with central disks, and probably rejuvenated, such as the BSF Es (and the other types of low-mass Es). Although their simulated galaxies are bulge dominated, they show very low Sérsic indexes (mostly $n < 2$), whereas our E galaxies, including the BSFs, show mostly $n > 2.5$ (see Fig. 6). For the MaNGA Es, the central disk structure is evident in BSFs ($\geq 93\%$), partially in the RQEs ($\sim 40\%$), and marginally in the CLEs ($< 20\%$).

Finally, we do not find very massive BSF galaxies. The rejuvenation process is likely quite inefficient in massive galaxies due to halo mass quenching (e.g., Zu & Mandelbaum 2016; and references therein) and the effects of feedback from strong AGNs.

7. Summary and conclusions

We have studied a sample of 343 E galaxies observed with the MaNGA survey (MPL-7). The morphological classification was done using the deep images of the DESI Legacy Imaging Surveys. We defined seven classes of E galaxies based on their integrated

spectroscopically properties from MaNGA and their colors from SDSS photometry. We paid attention to the CLE, RQE, and BSF types, which correspond to the classical ‘red and dead’ (73%), recently quenched (10%) and blue, star-forming (4%) E galaxies, respectively. We inferred for them the mass-weighted and luminosity-weighted stellar age and metallicity gradients, the sSFR radial profiles, and we reconstructed their integrated and radial CMTDs and specific SFHs. The results are presented and analyzed in mass bins so that effects due to volume incompleteness are minimized. Our main results can be summarized as follows.

- The CLEs show mild negative luminosity-weighted age gradients ($-0.08^{+0.06}_{-0.07} \text{ dex}/R_{eff}$), nearly flat mass-weighted age gradients ($-0.03^{+0.04}_{-0.05} \text{ dex}/R_{eff}$), and mildly steep negative gradients in both luminosity- and mass-weighted metallicities ($-0.11^{+0.06}_{-0.07} \text{ dex}/R_{eff}$ and $-0.11^{+0.07}_{-0.08} \text{ dex}/R_{eff}$, respectively). The CLEs accumulated 90% of their stellar masses between 5 and 7 Gyr ago. We observe a ‘downsizing’ trend in both stellar mass growth rates and SF quenching, i.e., the most massive CLEs tend to form stars earlier and quench faster than the less massive CLE galaxies. In general, the CLEs quench relatively fast, roughly in half the cosmic time at which they attained their most active phase of SF as traced by their luminosity-weighted ages. The CLEs show a weak inside-out formation assembly: their inner parts assembled 90% of their mass ~ 2 Gyr earlier than their external parts. This effect is more pronounced for massive ($M_\star > 10^{11} M_\odot$) galaxies. The radial specific SFHs show the quenching is faster in the inner parts compared to the outer parts, especially for the low-mass CLEs ($M_\star < 10^{10.4} M_\odot$).

- The RQE galaxies are ~ 4 – 5 Gyr younger than the CLEs using the light-weighted ages (by construction) and ~ 3 – 4 Gyr using mass-weighted stellar ages. The median gradients in stellar age and metallicity of the RQEs are similar or flatter, but with much larger scatter, than those of the CLEs of the same mass, except the massive ($M_\star > 10^{11} M_\odot$) RQEs that show positive median gradients in age_{lw} ($0.11^{+0.47}_{-0.37} \text{ dex}/R_{eff}$), Z_{lw} ($0.09^{+0.11}_{-0.06} \text{ dex}/R_{eff}$), and Z_{mw} ($0.07^{+0.07}_{-0.08} \text{ dex}/R_{eff}$). The RQE galaxies reached 90% of their total mass between 2 and 6 Gyr ago without a clear trend with mass. On average, they quenched 1.2 ± 0.9 Gyr ago and very fast, in less than 1/4th the cosmic time at which they attained the most active SF phase. For the less massive RQE galaxies, their inner parts show some evidence of earlier mass assembly than the outer parts, while for the most massive RQEs, the assembly is nearly homogeneous or slightly outside in some cases. Furthermore, the less massive RQEs show evidence of very weak inside-out quenching. Instead, the massive RQEs tend to show a mild outside-in quenching.

- The BSF E galaxies are younger at all radii than the CLEs using both age_{lw} and age_{mw} ; the differences are much larger for the former case, showing that BSFs suffered late bursts of SF. Their age and metallicity profiles are on average flatter than those of the CLEs. While their CMTDs and specific SFHs at early epochs are similar to those of CLEs of the same mass, overall they formed a significant fraction of their stellar mass at later times. For them, 90% of the total mass has been accumulated between 2 and 4 Gyr ago and they are still forming stars actively. Their specific SFHs remain nearly constant since 4–5 Gyr ago. We find that nearly all the BSFs have evidence of disky central structures. There are not massive BSF galaxies.

The results from our archaeological analysis of the CLE galaxies are consistent with a two-phase scenario, where these galaxies formed their (dominant in mass) central part early and nearly coeval, likely by gas-rich dissipative collapse, com-

paction, and a consequent intense burst of SF. As the SF is rapidly quenched by gas exhaustion (and probably, by AGN feedback), mergers (mostly dry) could have contributed to the assembly of the observed external parts of a significant fraction of CLEs.

We found that most of the properties of RQEs more massive than $M_\star \sim 10^{11} M_\odot$ differ from those of the less massive RQEs. For BSFs, we discussed the possibility that they formed early similarly as the CLEs of similar masses and then suffered a process of rejuvenation. There are not very massive BSFs, suggesting that the rejuvenation process is quite inefficient in massive galaxies.

We stress that the generic evolutionary interpretations discussed here for RQEs and BSF ellipticals could be flawed by the low numbers in our samples or the large diversity of their evolutionary paths. A case-by-case spectroscopic, photometric, and environmental analysis is desirable to confirm or modify these interpretations. We will report this analysis elsewhere.

Acknowledgements. We acknowledge the anonymous referee for his/her thoughtful revision of our paper. V.A.-R. acknowledges support from the projects CONACyT CB285721 and PAPIIT-UNAM IA104118. S.F.S. acknowledges support from the projects Conacyt CB285080, FC-2016-01-1916 and PAPIIT IN100519. This research made use of Montage. It is funded by the National Science Foundation under Grant Number ACI-1440620, and was previously funded by the National Aeronautics and Space Administration's Earth Science Technology Office, Computation Technologies Project, under Cooperative Agreement Number NCC5-626 between NASA and the California Institute of Technology. This research also made use of ASTROPY, a community-developed core PYTHON (<http://www.python.org>) package for Astronomy (Astropy Collaboration et al. 2013); MATPLOTLIB (Hunter 2007); NUMPY (Walt et al. 2011); PANDAS (McKinney 2010); and SCIPY (Jones et al. 2001). Funding for the Sloan Digital Sky Survey IV has been provided by the Alfred P. Sloan Foundation, the U.S. Department of Energy Office of Science, and the Participating Institutions. SDSS-IV acknowledges support and resources from the Center for High-Performance Computing at the University of Utah. The SDSS web site is www.sdss.org. SDSS-IV is managed by the Astrophysical Research Consortium for the Participating Institutions of the SDSS Collaboration including the Brazilian Participation Group, the Carnegie Institution for Science, Carnegie Mellon University, the Chilean Participation Group, the French Participation Group, Harvard-Smithsonian Center for Astrophysics, Instituto de Astrofísica de Canarias, The Johns Hopkins University, Kavli Institute for the Physics and Mathematics of the Universe (IPMU) / University of Tokyo, the Korean Participation Group, Lawrence Berkeley National Laboratory, Leibniz Institut für Astrophysik Potsdam (AIP), Max-Planck-Institut für Astronomie (MPIA Heidelberg), Max-Planck-Institut für Astrophysik (MPA Garching), Max-Planck-Institut für Extraterrestrische Physik (MPE), National Astronomical Observatories of China, New Mexico State University, New York University, University of Notre Dame, Observatório Nacional / MCTI, The Ohio State University, Pennsylvania State University, Shanghai Astronomical Observatory, United Kingdom Participation Group, Universidad Nacional Autónoma de México, University of Arizona, University of Colorado Boulder, University of Oxford, University of Portsmouth, University of Utah, University of Virginia, University of Washington, University of Wisconsin, Vanderbilt University, and Yale University. The Legacy Surveys consist of three individual and complementary projects: the Dark Energy Camera Legacy Survey (DECaLS; NOAO Proposal ID 2014B-0404; PIs: David Schlegel and Arjun Dey), the Beijing-Arizona Sky Survey (BASS; NOAO Proposal ID 2015A-0801; PIs: Zhou Xu and Xiaohui Fan), and the Mayall z-band Legacy Survey (MzLS; NOAO Proposal ID 2016A-0453; PI: Arjun Dey). DECaLS, BASS and MzLS together include data obtained, respectively, at the Blanco telescope, Cerro Tololo Inter-American Observatory, National Optical Astronomy Observatory (NOAO); the Bok telescope, Steward Observatory, University of Arizona; and the Mayall telescope, Kitt Peak National Observatory, NOAO. The Legacy Surveys project is honored to be permitted to conduct astronomical research on Iolkam Du'ag (Kit Peak), a mountain with particular significance to the Tohono O'odham Nation. NOAO is operated by the Association of Universities for Research in Astronomy (AURA) under a cooperative agreement with the National Science Foundation. This project used data obtained with the Dark Energy Camera (DECam), which was constructed by the Dark Energy Survey (DES) collaboration. Funding for the DES Projects has been provided by the U.S. Department of Energy, the U.S. National Science Foundation, the Ministry of Science and Education of Spain, the Science and Technology Facilities Council of the United Kingdom, the Higher Education Funding Council for England, the National Center for Supercomputing Applications at the University of Illinois at Urbana-Champaign, the Kavli Institute of Cosmological Physics at the Uni-

versity of Chicago, Center for Cosmology and Astro-Particle Physics at the Ohio State University, the Mitchell Institute for Fundamental Physics and Astronomy at Texas A&M University, Financiadora de Estudos e Projetos, Fundação Carlos Chagas Filho de Amparo, Financiadora de Estudos e Projetos, Fundação Carlos Chagas Filho de Amparo a Pesquisa do Estado do Rio de Janeiro, Conselho Nacional de Desenvolvimento Científico e Tecnológico and the Ministerio da Ciencia, Tecnología e Inovacão, the Deutsche Forschungsgemeinschaft and the Collaborating Institutions in the Dark Energy Survey. The Collaborating Institutions are Argonne National Laboratory, the University of California at Santa Cruz, the University of Cambridge, Centro de Investigaciones Energeticas, Medioambientales y Tecnologicas-Madrid, the University of Chicago, University College London, the DES-Brazil Consortium, the University of Edinburgh, the Eidgenössische Technische Hochschule (ETH) Zurich, Fermi National Accelerator Laboratory, the University of Illinois at Urbana-Champaign, the Institut de Ciencias de l'Espai (IEEC/CSIC), the Institut de Fisica d'Altes Energies, Lawrence Berkeley National Laboratory, the Ludwig-Maximilians-Universität München and the associated Excellence Cluster Universe, the University of Michigan, the National Optical Astronomy Observatory, the University of Nottingham, the Ohio State University, the University of Pennsylvania, the University of Portsmouth, SLAC National Accelerator Laboratory, Stanford University, the University of Sussex, and Texas A&M University. BASS is a key project of the Telescope Access Program (TAP), which has been funded by the National Astronomical Observatories of China, the Chinese Academy of Sciences (the Strategic Priority Research Program "The Emergence of Cosmological Structures" Grant XDB09000000), and the Special Fund for Astronomy from the Ministry of Finance. The BASS is also supported by the External Cooperation Program of Chinese Academy of Sciences (Grant 114A11KYSB20160057), and Chinese National Natural Science Foundation (Grant 11433005). The Legacy Survey team makes use of data products from the Near-Earth Object Wide-field Infrared Survey Explorer (NEOWISE), which is a project of the Jet Propulsion Laboratory/California Institute of Technology. NEOWISE is funded by the National Aeronautics and Space Administration. The Legacy Surveys imaging of the DESI footprint is supported by the Director, Office of Science, Office of High Energy Physics of the U.S. Department of Energy under Contract No. DE-AC02-05CH1123, by the National Energy Research Scientific Computing Center, a DOE Office of Science User Facility under the same contract; and by the U.S. National Science Foundation, Division of Astronomical Sciences under Contract No. AST-0950945 to NOAO.

References

Aguado, D. S., Ahumada, R., Almeida, A., et al. 2019, *ApJS*, 240, 23
 Aquino-Ortíz, E., Valenzuela, O., Sánchez, S. F., et al. 2018, *MNRAS*, 479, 2133
 Argudo-Fernández, M., Lacerna, I., & Duarte Puertas, S. 2018, *A&A*, 620, A113
 Astro Collaboration, Robitaille, T. P., Tollerud, E. J., et al. 2013, *A&A*, 558, A33
 Avila-Reese, V., González-Samaniego, A., Colín, P., Ibarra-Medel, H., & Rodríguez-Puebla, A. 2018, *ApJ*, 854, 152
 Avila-Reese, V., Zavala, J., & Lacerna, I. 2014, *MNRAS*, 441, 417
 Bacon, R., Copin, Y., Monnet, G., et al. 2001, *MNRAS*, 326, 23
 Baldwin, J. A., Phillips, M. M., & Terlevich, R. 1981, *PASP*, 93, 5
 Bamford, S. P., Nichol, R. C., Baldry, I. K., et al. 2009, *MNRAS*, 393, 1324
 Barone, T. M., D'Eugenio, F., Colless, M., et al. 2018, *ApJ*, 856, 64
 Bassett, R., Bekki, K., Cortese, L., et al. 2017, *MNRAS*, 470, 1991
 Belfiore, F., Maiolino, R., Bundy, K., et al. 2018, *MNRAS*, 477, 3014
 Bell, E. F., McIntosh, D. H., Katz, N., & Weinberg, M. D. 2003, *ApJS*, 149, 289
 Belluzzi, E., Ascasibar, Y., Galbany, L., et al. 2019, *A&A*, 625, A83
 Bernardi, M., Domínguez Sánchez, H., Brownstein, J. R., Drory, N., & Sheth, R. K. 2019, *MNRAS*, 489, 5633
 Bernardi, M., Nichol, R. C., Sheth, R. K., Miller, C. J., & Brinkmann, J. 2006, *AJ*, 131, 1288
 Binney, J. & Merrifield, M. 1998, *Galactic Astronomy*
 Bitsakis, T., Sánchez, S. F., Ciesla, L., et al. 2019, *MNRAS*, 483, 370
 Blanton, M. R., Bershady, M. A., Abolfathi, B., et al. 2017, *AJ*, 154, 28
 Bluck, A. F. L., Maiolino, R., Sánchez, S. F., et al. 2020, *MNRAS*, 492, 96
 Bluck, A. F. L., Mendel, J. T., Ellison, S. L., et al. 2016, *MNRAS*, 462, 2559
 Boardman, N. F., Weijmans, A.-M., van den Bosch, R., et al. 2017, *MNRAS*, 471, 4005
 Brinchmann, J., Charlot, S., White, S. D. M., et al. 2004, *MNRAS*, 351, 1151
 Bundy, K., Bershady, M. A., Law, D. R., et al. 2015, *ApJ*, 798, 7
 Cano-Díaz, M., Ávila-Reese, V., Sánchez, S. F., et al. 2019, *MNRAS*, 1830
 Cano-Díaz, M., Sánchez, S. F., Zibetti, S., et al. 2016, *ApJ*, 821, L26
 Cappellari, M. 2016, *ARA&A*, 54, 597
 Cappellari, M., Emsellem, E., Krajnović, D., et al. 2011a, *MNRAS*, 413, 813
 Cappellari, M., Emsellem, E., Krajnović, D., et al. 2011b, *MNRAS*, 416, 1680
 Cardelli, J. A., Clayton, G. C., & Mathis, J. S. 1989, *ApJ*, 345, 245
 Carnall, A. C., McLure, R. J., Dunlop, J. S., & Davé, R. 2018, *MNRAS*, 480, 4379

Cheng, J. Y., Faber, S. M., Simard, L., et al. 2011, MNRAS, 412, 727

Cherinka, B., Andrews, B. H., Sánchez-Gallego, J., et al. 2019, AJ, 158, 74

Cibinel, A., Carollo, C. M., Lilly, S. J., et al. 2013, ApJ, 776, 72

Cook, B. A., Conroy, C., Pillepich, A., Rodriguez-Gomez, V., & Hernquist, L. 2016, ApJ, 833, 158

Croom, S. M., Lawrence, J. S., Bland-Hawthorn, J., et al. 2012, MNRAS, 421, 872

Crossett, J. P., Pimbblet, K. A., Stott, J. P., & Jones, D. H. 2014, MNRAS, 437, 2521

Darg, D. W., Kaviraj, S., Lintott, C. J., et al. 2010, MNRAS, 401, 1552

Davis, T. A. & Bureau, M. 2016, MNRAS, 457, 272

de Zeeuw, P. T., Bureau, M., Emsellem, E., et al. 2002, MNRAS, 329, 513

Dekel, A. & Burkert, A. 2014, MNRAS, 438, 1870

Dey, A., Schlegel, D. J., Lang, D., et al. 2019, AJ, 157, 168

Di Matteo, P., Pipino, A., Lehnert, M. D., Combes, F., & Semelin, B. 2009, A&A, 499, 427

Domínguez Sánchez, H., Bernardi, M., Brownstein, J. R., Drory, N., & Sheth, R. K. 2019, MNRAS, 489, 5612

Domínguez Sánchez, H., Bernardi, M., Nikakhtar, F., Margalef-Bentabol, B., & Sheth, R. K. 2020, MNRAS, 495, 2894

Dressler, A. 1980, ApJ, 236, 351

Drory, N., MacDonald, N., Bershady, M. A., et al. 2015, AJ, 149, 77

Ellison, S. L., Sánchez, S. F., Ibarra-Medel, H., et al. 2018, MNRAS, 474, 2039

Emsellem, E., Cappellari, M., Krajnović, D., et al. 2011, MNRAS, 414, 888

Emsellem, E., Cappellari, M., Krajnović, D., et al. 2007, MNRAS, 379, 401

Ferreras, I., Scott, N., Barbera, F. L., et al. 2019, MNRAS, 2057

Firmani, C. & Avila-Reese, V. 2010, ApJ, 723, 755

Fisher, D. B. & Drory, N. 2011, ApJ, 733, L47

Gadotti, D. A. 2009, MNRAS, 393, 1531

Gallazzi, A., Charlot, S., Brinchmann, J., White, S. D. M., & Tremonti, C. A. 2005, MNRAS, 362, 41

García-Benito, R., González Delgado, R. M., Pérez, E., et al. 2017, A&A, 608, A27

George, K. & Zingade, K. 2015, A&A, 583, A103

Goddard, D., Thomas, D., Maraston, C., et al. 2017, MNRAS, 466, 4731

González Delgado, R. M., Cerviño, M., Martins, L. P., Leitherer, C., & Hauschildt, P. H. 2005, MNRAS, 357, 945

González Delgado, R. M. & Cid Fernandes, R. 2010, MNRAS, 403, 797

González Delgado, R. M., García-Benito, R., Pérez, E., et al. 2015, A&A, 581, A103

González Delgado, R. M., Pérez, E., Cid Fernandes, R., et al. 2017, A&A, 607, A128

Graham, A. W. 2019, MNRAS, 487, 4995

Graham, M. T., Cappellari, M., Li, H., et al. 2018, MNRAS, 477, 4711

Gunn, J. E., Siegmund, W. A., Mannery, E. J., et al. 2006, AJ, 131, 2332

Guo, K., Peng, Y., Shao, L., et al. 2019, ApJ, 870, 19

Hernández-Toledo, H. M., Vázquez-Mata, J. A., Martínez-Vázquez, L. A., et al. 2008, AJ, 136, 2115

Hernández-Toledo, H. M., Vázquez-Mata, J. A., Martínez-Vázquez, L. A., Choi, Y.-Y., & Park, C. 2010, AJ, 139, 2525

Hernquist, L. 1993, ApJ, 409, 548

Hirschmann, M., Naab, T., Ostriker, J. P., et al. 2015, MNRAS, 449, 528

Holden, B. P., van der Wel, A., Rix, H.-W., & Franx, M. 2012, ApJ, 749, 96

Hood, C. E., Kannappan, S. J., Stark, D. V., et al. 2018, ApJ, 857, 144

Hopkins, P. F., Cox, T. J., Dutta, S. N., et al. 2009, ApJS, 181, 135

Hubble, E. P. 1936, Realm of the Nebulae

Hunter, J. D. 2007, Computing In Science & Engineering, 9, 90

Ibarra-Medel, H. J., Avila-Reese, V., Sánchez, S. F., González-Samaniego, A. r., & Rodríguez-Puebla, A. 2019, MNRAS, 483, 4525

Ibarra-Medel, H. J., Sánchez, S. F., Avila-Reese, V., et al. 2016, MNRAS, 463, 2799

Jones, E., Oliphant, T., Peterson, P., et al. 2001, SciPy: Open source scientific tools for Python, [Online; accessed 2016-01-15]

Kannappan, S. J., Guie, J. M., & Baker, A. J. 2009, AJ, 138, 579

Kauffmann, G., Heckman, T. M., White, S. D. M., et al. 2003, MNRAS, 341, 33

Kewley, L. J., Dopita, M. A., Sutherland, R. S., Heisler, C. A., & Trevena, J. 2001, ApJ, 556, 121

Kobayashi, C. 2004, MNRAS, 347, 740

Koleva, M., Prugniel, P., De Rijcke, S., & Zeilinger, W. W. 2011, MNRAS, 417, 1643

Kormendy, J. 2016, in Astrophysics and Space Science Library, Vol. 418, Galactic Bulges, ed. E. Laurikainen, R. Peletier, & D. Gadotti, 431

Kormendy, J., Fisher, D. B., Cornell, M. E., & Bender, R. 2009, ApJS, 182, 216

Kroupa, P. 2001, MNRAS, 322, 231

Kuntschner, H., Emsellem, E., Bacon, R., et al. 2010, MNRAS, 408, 97

Kuntschner, H., Smith, R. J., Colless, M., et al. 2002, MNRAS, 337, 172

Lacerna, I., Argudo-Fernández, M., & Duarte Puetas, S. 2018, A&A, 620, A117

Lacerna, I., Hernández-Toledo, H. M., Avila-Reese, V., Abenza-Sane, J., & del Olmo, A. 2016, A&A, 588, A79

Lacerna, I., Rodríguez-Puebla, A., Avila-Reese, V., & Hernández-Toledo, H. M. 2014, ApJ, 788, 29

Lagos, C. d. P., Davis, T. A., Lacey, C. G., et al. 2014, MNRAS, 443, 1002

Larson, R. B. 1974, MNRAS, 166, 585

Law, D. R., Cherinka, B., Yan, R., et al. 2016, AJ, 152, 83

Law, D. R., Yan, R., Bershady, M. A., et al. 2015, AJ, 150, 19

Lee, J. H., Lee, M. G., & Hwang, H. S. 2006, ApJ, 650, 148

Li, H., Mao, S., Cappellari, M., et al. 2018, MNRAS, 476, 1765

Lin, L., Hsieh, B.-C., Pan, H.-A., et al. 2019, ApJ, 872, 50

López-Cobá, C., Sánchez, S. F., Anderson, J. P., et al. 2020, AJ, 159, 167

López Fernández, R., González Delgado, R. M., Pérez, E., et al. 2018, A&A, 615, A27

Ma, C.-P., Greene, J. E., McConnell, N., et al. 2014, ApJ, 795, 158

Malin, D. F. & Carter, D. 1983, ApJ, 274, 534

Mancillas, B., Duc, P.-A., Combes, F., et al. 2019, A&A, 632, A122

Martig, M., Bournaud, F., Teyssier, R., & Dekel, A. 2009, ApJ, 707, 250

Martín-Navarro, I., Vazdekis, A., Falcón-Barroso, J., et al. 2018, MNRAS, 475, 3700

McDermid, R. M., Alatalo, K., Blitz, L., et al. 2015, MNRAS, 448, 3484

McIntosh, D. H., Wagner, C., Cooper, A., et al. 2014, MNRAS, 442, 533

McKinney, W. 2010, in Proceedings of the 9th Python in Science Conference, ed. S. van der Walt & J. Millman, 51 – 56

Mo, H., van den Bosch, F. C., & White, S. 2010, Galaxy Formation and Evolution

Muzzin, A., Marchesini, D., Stefanon, M., et al. 2013, ApJ, 777, 18

Naab, T., Johansson, P. H., & Ostriker, J. P. 2009, ApJ, 699, L178

Naab, T., Oser, L., Emsellem, E., et al. 2014, MNRAS, 444, 3357

Nair, P. B. & Abraham, R. G. 2010, ApJS, 186, 427

Navarro-González, J., Ricciardelli, E., Quilis, V., & Vazdekis, A. 2013, MNRAS, 436, 3507

Oemler, Jr., A. 1974, ApJ, 194, 1

Oser, L., Ostriker, J. P., Naab, T., Johansson, P. H., & Burkert, A. 2010, ApJ, 725, 2312

Oyarzún, G. A., Bundy, K., Westfall, K. B., et al. 2019, ApJ, 880, 111

Pacifci, C., Kassin, S. A., Weiner, B. J., et al. 2016, ApJ, 832, 79

Pandya, V., Brennan, R., Somerville, R. S., et al. 2017, MNRAS, 472, 2054

Parikh, T., Thomas, D., Maraston, C., et al. 2019, Monthly Notices of the Royal Astronomical Society, 483, 3420

Peek, J. E. G. & Graves, G. J. 2010, ApJ, 719, 415

Pipino, A., D'Ercole, A., Chiappini, C., & Matteucci, F. 2010, MNRAS, 407, 1347

Pipino, A., D'Ercole, A., & Matteucci, F. 2008, A&A, 484, 679

Plauchu-Frayn, I., Del Olmo, A., Coziol, R., & Torres-Papaqui, J. P. 2012, A&A, 546, A48

Rawle, T. D., Smith, R. J., & Lucey, J. R. 2010, Monthly Notices of the Royal Astronomical Society, 401, 852

Rawle, T. D., Smith, R. J., Lucey, J. R., & Swinbank, A. M. 2008, MNRAS, 389, 1891

Reda, F. M., Proctor, R. N., Forbes, D. A., Hau, G. K. T., & Larsen, S. S. 2007, MNRAS, 377, 1772

Rodríguez-Gómez, V., P illepich, A., Sales, L. V., et al. 2016, MNRAS, 458, 2371

Rosito, M. S., Pedrosa, S. E., Tissera, P. B., et al. 2018, A&A, 614, A85

Rosito, M. S., Tissera, P. B., Pedrosa, S. E., & Lagos, C. D. P. 2019a, A&A, 629, L3

Rosito, M. S., Tissera, P. B., Pedrosa, S. E., & Rosas-Guevara, Y. 2019b, A&A, 629, A37

Salim, S., Rich, R. M., Charlot, S., et al. 2007, ApJS, 173, 267

Salpeter, E. E. 1955, ApJ, 121, 161

San Roman, I., Cenarro, A. J., Díaz-García, L. A., et al. 2018, A&A, 609, A20

Sánchez, S. F. 2020, ARA&A, 58, 99

Sánchez, S. F., Avila-Reese, V., Hernandez-Toledo, H., et al. 2018, Rev. Mexicana Astron. Astrofis., 54, 217

Sánchez, S. F., Avila-Reese, V., Rodríguez-Puebla, A., et al. 2019, MNRAS, 482, 1557

Sánchez, S. F., Barrera-Ballesteros, J. K., Sánchez-Menguiano, L., et al. 2017, MNRAS, 469, 2121

Sánchez, S. F., Kennicutt, R. C., Gil de Paz, A., et al. 2012, A&A, 538, A8

Sánchez, S. F., Pérez, E., Sánchez-Blázquez, P., et al. 2016a, Rev. Mexicana Astron. Astrofis., 52, 21

Sánchez, S. F., Pérez, E., Sánchez-Blázquez, P., et al. 2016b, Rev. Mexicana Astron. Astrofis., 52, 171

Sánchez, S. F., Rosales-Ortega, F. F., Iglesias-Páramo, J., et al. 2014, A&A, 563, A49

Sánchez-Blázquez, P., Forbes, D. A., Strader, J., Brodie, J., & Proctor, R. 2007, MNRAS, 377, 759

Sánchez-Menguiano, L., Sánchez, S. F., Pérez, I., et al. 2018, A&A, 609, A119

Sarzi, M., Falcón-Barroso, J., Davies, R. L., et al. 2006, MNRAS, 366, 1151

Scalo, J. M. 1986, Fund. Cosmic Phys., 11, 1

Schawinski, K., Lintott, C., Thomas, D., et al. 2009, MNRAS, 396, 818

Schawinski, K., Thomas, D., Sarzi, M., et al. 2007, MNRAS, 382, 1415

Schawinski, K., Urry, C. M., Simmons, B. D., et al. 2014, MNRAS, 440, 889

Schweizer, F. & Seitzer, P. 1992, AJ, 104, 1039

Shapiro, K. L., Falcón-Barroso, J., van de Ven, G., et al. 2010, MNRAS, 402, 2140

Sheth, R. K. & Bernardi, M. 2012, MNRAS, 422, 1825

Smethurst, R. J., Lintott, C. J., Bamford, S. P., et al. 2017, MNRAS, 469, 3670

Smethurst, R. J., Lintott, C. J., Simmons, B. D., et al. 2015, MNRAS, 450, 435

Smethurst, R. J., Masters, K. L., Lintott, C. J., et al. 2018, MNRAS, 473, 2679

Smith, R. M., Fernández-Soto, A., Martínez, V., et al. 2010, in Astronomical Society of the Pacific Conference Series, Vol. 421, Galaxies in Isolation: Exploring Nature Versus Nurture, ed. L. Verdes-Montenegro, A. Del Olmo, & J. Sulentic, 221

Spector, O. & Brosch, N. 2017, MNRAS, 469, 347

Spolaor, M., Kobayashi, C., Forbes, D. A., Couch, W. J., & Hau, G. K. T. 2010, Monthly Notices of the Royal Astronomical Society, 408, 272

Strateva, I., Ivezić, Ž., Knapp, G. R., et al. 2001, AJ, 122, 1861

Suh, H., Jeong, H., Oh, K., et al. 2010, ApJS, 187, 374

Tabor, M., Merrifield, M., Aragón-Salamanca, A., et al. 2019, MNRAS, 485, 1546

Tacchella, S., Dekel, A., Carollo, C. M., et al. 2016, MNRAS, 458, 242

Taylor, P. & Kobayashi, C. 2017, MNRAS, 471, 3856

Thanjavur, K., Simard, L., Bluck, A. F. L., & Mendel, T. 2016, MNRAS, 459, 44

Thomas, D., Maraston, C., Schawinski, K., Sarzi, M., & Silk, J. 2010, MNRAS, 404, 1775

Toomre, A. 1977, in Evolution of Galaxies and Stellar Populations, ed. B. M. Tinsley & D. C. Larson, Richard B. Gehret, 401

Tremonti, C. A., Heckman, T. M., Kauffmann, G., et al. 2004, ApJ, 613, 898

Tutukov, A. V., Dryomov, V. V., & Dryomova, G. N. 2007, Astronomy Reports, 51, 435

van Dokkum, P. G. 2005, AJ, 130, 2647

Vazdekis, A., Sánchez-Blázquez, P., Falcón-Barroso, J., et al. 2010, MNRAS, 404, 1639

Veale, M., Ma, C.-P., Greene, J. E., et al. 2018, MNRAS, 473, 5446

Veilleux, S. & Osterbrock, D. E. 1987, ApJS, 63, 295

Vulcani, B., Poggianti, B. M., Fritz, J., et al. 2015, ApJ, 798, 52

Wake, D. A., Bundy, K., Diamond-Stanic, A. M., et al. 2017, AJ, 154, 86

Walt, S. v. d., Colbert, S. C., & Varoquaux, G. 2011, Computing in Science & Engineering, 13, 22

Westfall, K. B., Cappellari, M., Bershady, M. A., et al. 2019, AJ, 158, 231

Whitaker, K. E., van Dokkum, P. G., Brammer, G., et al. 2013, ApJ, 770, L39

White, S. D. M. 1978, MNRAS, 184, 185

Wilkinson, D. M., Maraston, C., Goddard, D., Thomas, D., & Parikh, T. 2017, MNRAS, 472, 4297

Wu, P.-F., van der Wel, A., Bezanson, R., et al. 2020, ApJ, 888, 77

Yeruf, H. M., Faber, S. M., Trump, J. R., et al. 2014, ApJ, 792, 84

Young, L. M., Scott, N., Serra, P., et al. 2014, MNRAS, 444, 3408

Zheng, Z., Wang, H., Ge, J., et al. 2017, Monthly Notices of the Royal Astronomical Society, 465, 4572

Zibetti, S., Gallazzi, A. R., Hirschmann, M., et al. 2020, MNRAS, 491, 3562

Zu, Y. & Mandelbaum, R. 2016, MNRAS, 457, 4360

Appendix A: Individual age profiles

We discussed in Sect. 6 that there is a diversity of radial trends reported in the literature for the stellar age profiles. Different softwares, stellar population models, and methods to derive the stellar age gradients may explain the diversity of results. Here we do not pretend to make an exhaustive comparison of the methods, but we show our results for the same five galaxies in Fig. 7 of Goddard et al. (2017) as examples of radial profiles for individual galaxies rather than comparing average trends. Fig. A.1 shows our mass- and light-weighted age profiles for galaxies observed in MaNGA with a different number of fibers. The light-weighted age profiles (red lines) tend to be mildly negative or flat, which is consistent with the results of Goddard et al. (2017). However, our mass-weighted age profiles are also mildly negative or flat, which is opposite to the positive age gradients reported by Goddard et al. (2017).

A possible explanation for the different trends is that we weight by the stellar mass (or light) 2D maps within each radial bin. Fig. A.2 shows the radial profiles without this weighting (solid lines). We still obtain mildly negative or flat gradients regardless of the weighting approach. Furthermore, we do not see

evident positive gradients in the mass-weighted age maps (see Fig. A.3), i.e., the galaxy outskirts do not seem to be older than the internal parts.

There are other differences between Goddard et al. (2017) and our methods that may explain why we obtain opposite trends with the mass-weighted ages. They use inputs from the MaNGA data analysis pipeline (DAP, Westfall et al. 2019) for running their spectral fitting code FIREFLY (Wilkinson et al. 2017) with minimum S/N = 5 in the r -band, whereas we use Pipe3D with a threshold S/N = 50 for the segmentation and integrated within the V band. The most significant difference between FIREFLY and our results (Pipe3D) is that FIREFLY arithmetically average their light and mass weighed ages while Pipe3D uses a logarithmic average (see Eqs. 1–2), so the weight of young stars goes to zero in FIREFLY. Furthermore, there are many differences in the methodology to obtain the SSP decomposition: different stellar libraries, different extinction laws, different S/N definitions for saying the most important differences.

A depth exploratory comparison of the methods will be presented in a future paper.

Appendix B: Radial profiles with more than five bins

In Sect. 4 we show both individual and “stacked” radial profiles using only five radial bins in units of R_{eff} given the typical PSF size of MaNGA observations (see the horizontal error bars in panels of Figs. 8–10). Zibetti et al. (2020) have suggested the presence of a “U-shape” in the inner regions of the light-weighted stellar age profiles of E galaxies, with a minimum around $0.4 R_{\text{eff}}$, which is not present in our results. We here also calculate the radial profiles using twelve radial bins for each galaxy to see if the shape of the profiles shows some dependence on the radial binning. Fig B.1 corresponds to the mass-weighted and luminosity-weighted age profiles using twelve radial bins. Although we increased the number of bins, our analysis always considers the typical PSF size (horizontal error bar). The shapes of the profiles are similar to those shown in Fig. 8. We obtain similar results for the metallicity and sSFR profiles. Therefore, our trends do not change with a smaller radial bin. We do not observe an evident “U-shape” in the inner region of the age profiles of Es, which is consistent with others works (e.g., González Delgado et al. 2015; Zheng et al. 2017), although there is a tiny dip in the light-weighted age profiles at $\sim 0.2 R_{\text{eff}}$ only for low-mass Es. As discussed above, different softwares, stellar population models, and methods to derive the stellar age gradients may explain the diversity of results in the stellar age profiles.

Appendix C: Fine-Structure and kinematic morphological features

This section presents preliminary results after a uniform visual search for faint substructure in the BSF, RQE, and CLE galaxies using moderately-deep imaging from the DESI Legacy Imaging Surveys. We also inspected the central regions of CLE, RQE, and BSF galaxies to identify dusty non-regular features that may hint for the presence of central disks. Additionally, we extracted from the DAP products available in Marvin¹³ (Cherinka et al. 2019) the projected stellar rotation velocity, ionized gas rotation velocity and the EW(H α), corrected for underlying stellar continuum absorption.

¹³ <https://www.sdss.org/dr15/manga/marvin/>

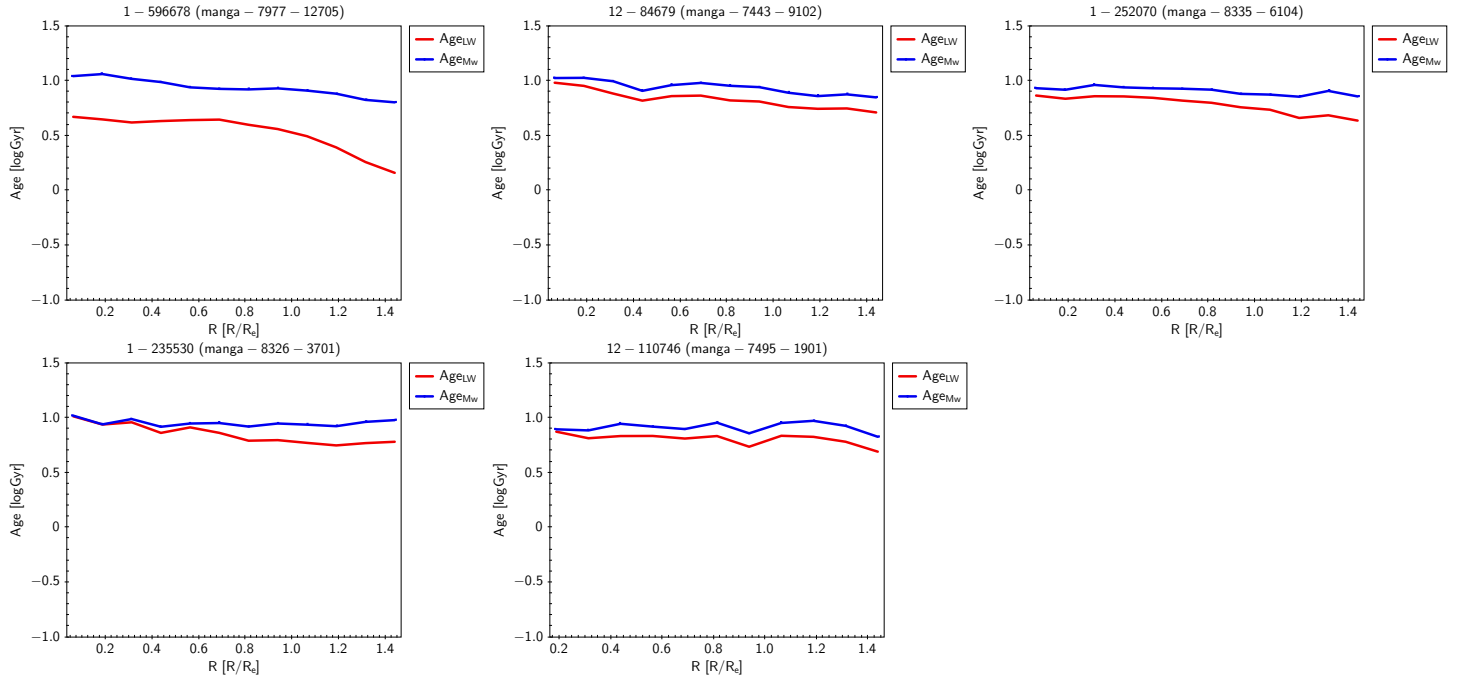


Fig. A.1. Our mass- and light-weighted age profiles (blue and red lines, respectively) for the galaxies in Fig. 7 of Goddard et al. (2017). The MaNGA ID and the Plate-IFU design are shown above each panel.

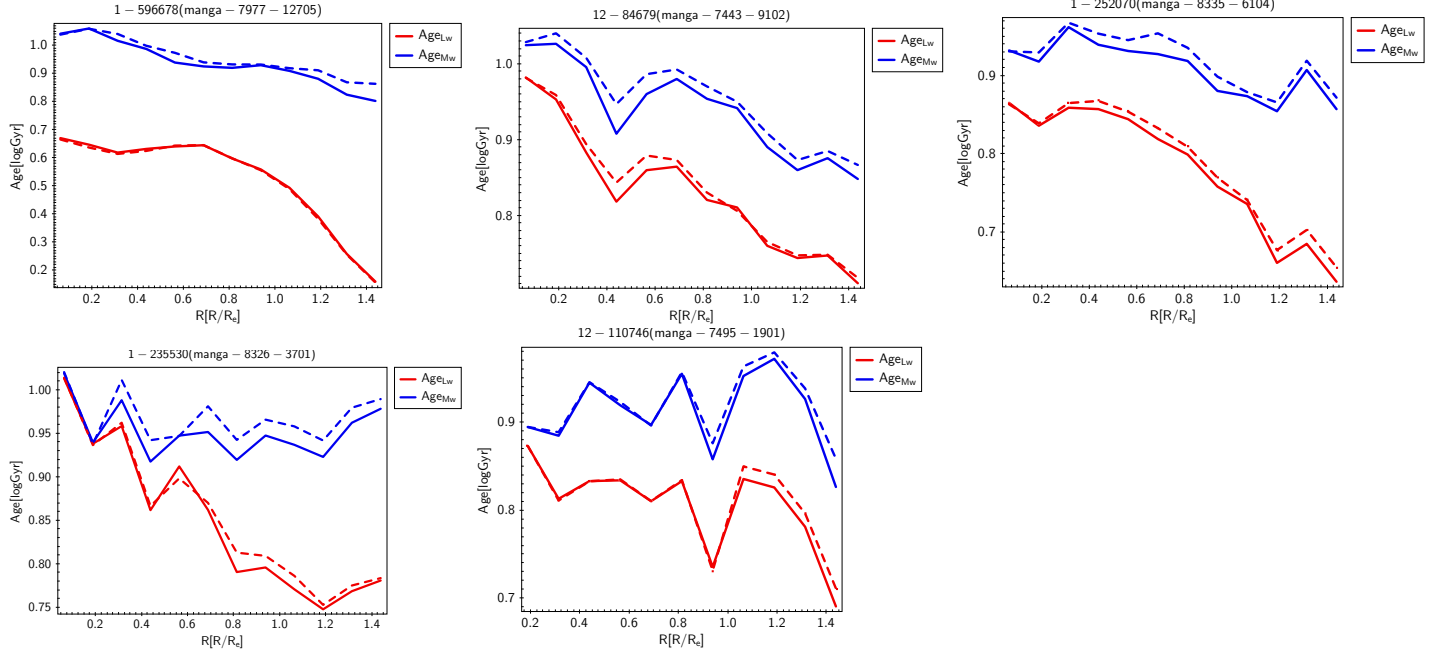


Fig. A.2. Our mass- and light-weighted age profiles (blue and red lines, respectively) for the galaxies in Fig. 7 of Goddard et al. (2017). The dashed lines are the same in Fig. A.1. The solid lines are the profiles without weighting by mass or light within each radial bin. The MaNGA ID and the Plate-IFU design are shown above each panel.

The BSF galaxies show evidence of dusty non-regular (disk-like) features in their central regions in practically all the cases (93%). This fraction amounts to 69% in RQEs and decreases drastically to 21% in CLEs. The spatial distribution of $\text{EW}(\text{H}\alpha)$ is very different between BSFs, RQEs, and CLEs. All (100%) BSF galaxies show a spatially dominant $\text{H}\alpha$ concentration in the central region of these galaxies, while in RQEs and CLEs, that happens with a relatively low frequency of 18% and 13%, respectively. The velocity maps show evidence of disk rotation in nearly all the BSF galaxies (93%), and this fraction decreases

to 31% for the RQE galaxies. In summary, the fraction of BSF galaxies with evidence of central disks is $\geq 93\%$, while this fraction is $\sim 40\%$ on average for the RQE galaxies.

We have taken advantage of the post-processing catalog by the DESI collaboration (Dey et al. 2019) to generate a census of fine morphological structures at a surface brightness limit of $27.5 \text{ mag arcsec}^{-2}$. We visually categorize these structures as broad tides, shells, and filaments or tidal streams. Here we report the incidence of broad tidal structures (fans and plumes), which emerge from the main body of the galaxy, and shells. The

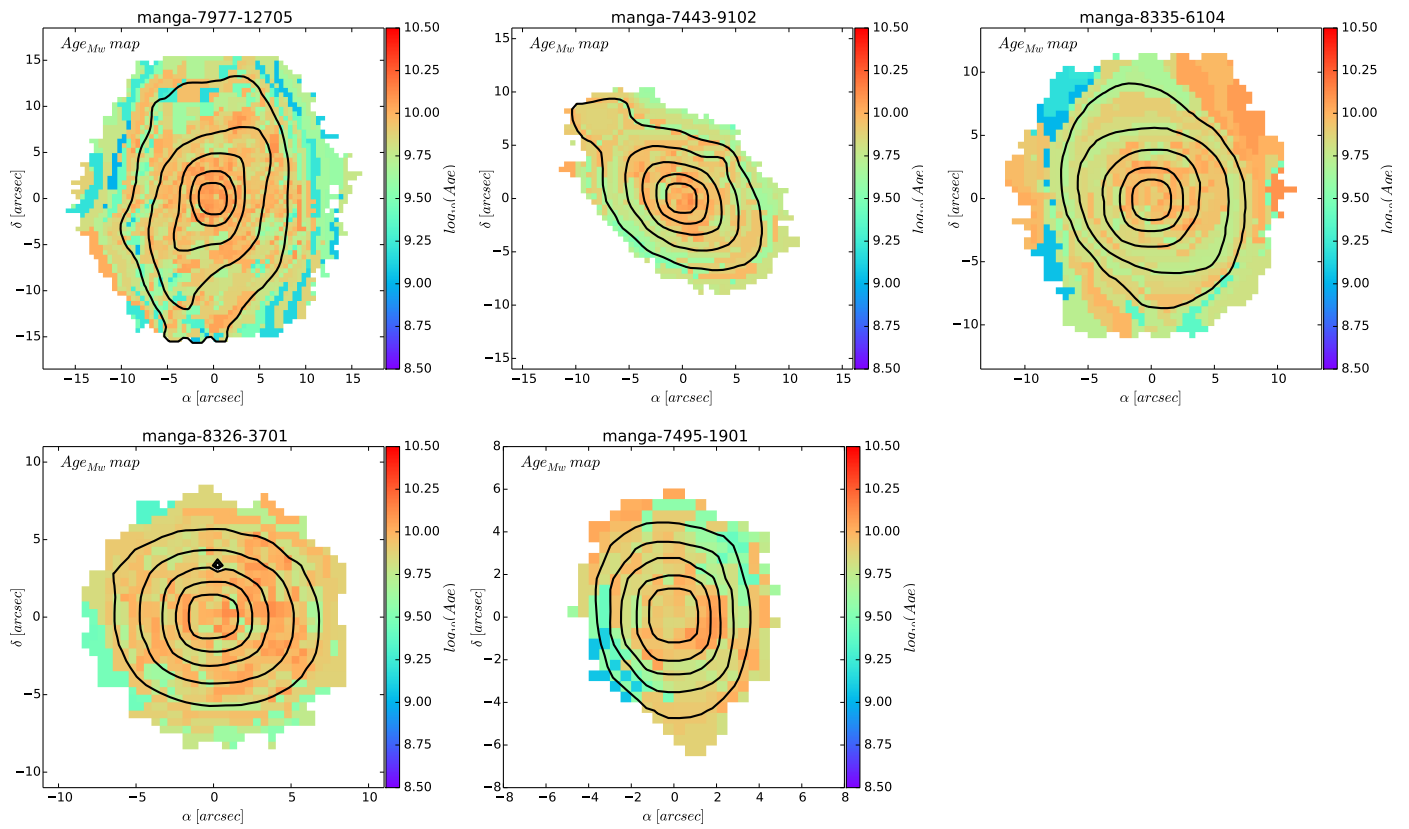


Fig. A.3. Our mass-weighted age maps for the galaxies in Fig. 7 of [Goddard et al. \(2017\)](#). The Plate-IFU design is shown above each panel.

incidence of filaments is very low in the three E galaxy samples. Broad tides result mostly from major or intermediate dry mergers and do not survive long times (e.g., [van Dokkum 2005; Mancillas et al. 2019](#)). Thus, if they are observed, then the merger was relatively recent. The shells are commonly found around E galaxies (e.g., [Malin & Carter 1983; Schweizer & Seitzer 1992](#)) and are the result of intermediate mergers that could have happened a long time ago, given that they can survive long times (up to several Gyr) if more recent mergers do not destroy them (e.g., [Mancillas et al. 2019](#)).

We report the incidence of broad tides and shells for each stellar mass bin employed in this paper: $\log(M_*/M_\odot) \geq 11.0$, $10.4 \leq \log(M_*/M_\odot) < 11.0$, and $9.4 \leq \log(M_*/M_\odot) < 10.4$, the high-, intermediate-, and low-mass bins, respectively.

For CLEs, the incidence of broad tides in these three mass bins is 65%, 43%, and 30%, respectively, while the respective incidences of shells are 24%, 31%, and 5%.

For RQEs, the incidence of broad tides in the three mass bins is 85%, 66%, and 11%, respectively, while the respective incidences of shells are 0%, 33%, and 5%.

For BSFs, there are not objects more massive than $10^{11} M_\odot$. The overall incidence of broad tides in this galaxy sample is of 30% (50% and 23% in the intermediate- and low-mass bins, respectively), while the overall incidence of shells is 48% (50% and 44%, respectively).

The reported fractions must be taken with caution, especially for the low-mass bin, in which mergers or interactions with other low-mass or dwarf galaxies produce features of very low-surface brightness. The visibility of fine structure features depends on the sample surface brightness limit and the galaxy orientation ([Mancillas et al. 2019](#)).

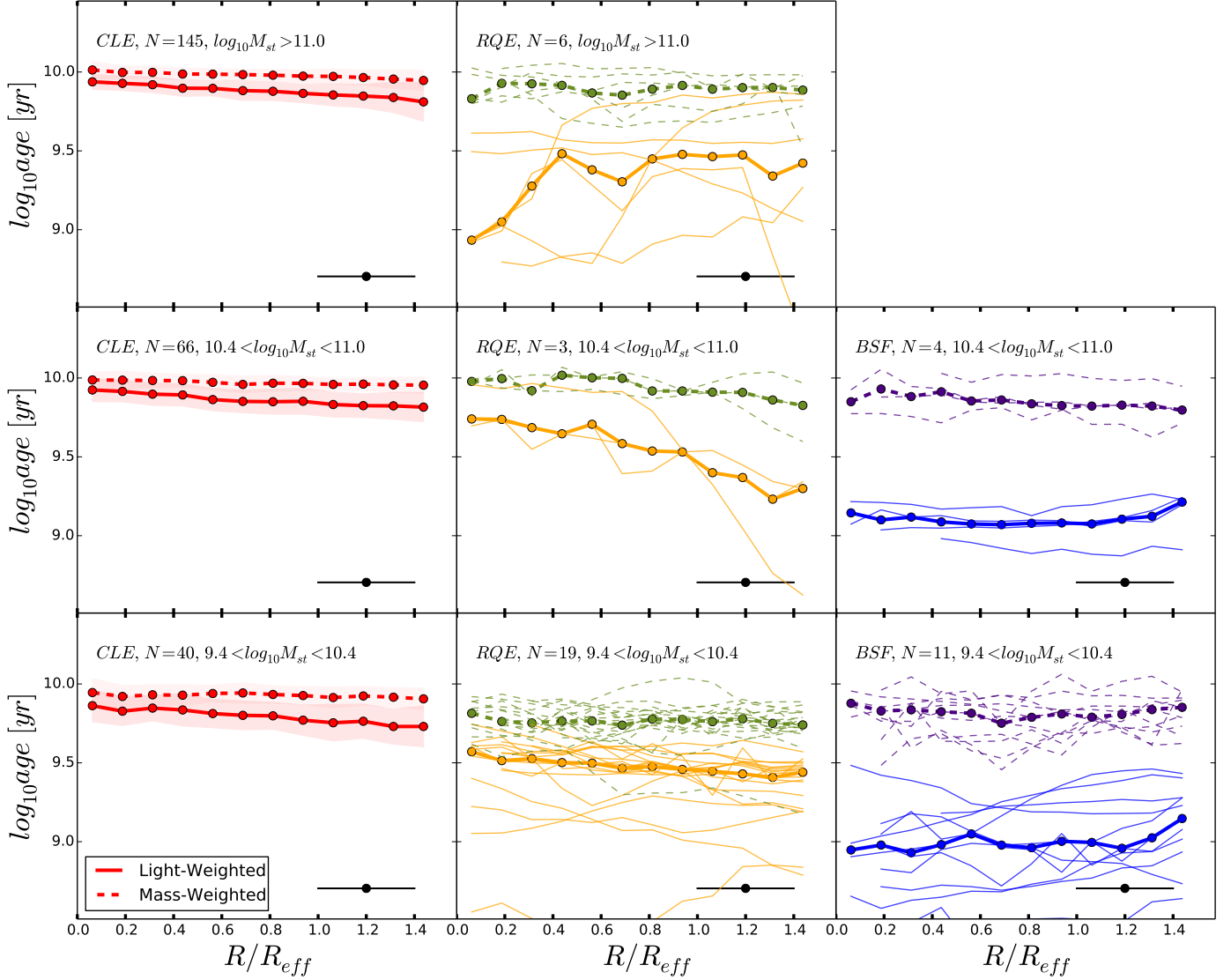


Fig. B.1. Similar to Fig. 8 but using 12 radial bins.